science.sciencemag.org/cgi/content/full/science.abc3660/DC1

Supplementary Materials for

Variations in color and reflectance on the surface of asteroid (101955) Bennu

D. N. DellaGiustina*, K. N. Burke, K. J. Walsh, P. H. Smith, D. R. Golish, E. B. Bierhaus, R.-L. Ballouz, T. L. Becker, H. Campins, E. Tatsumi, K. Yumoto, S. Sugita, J. D. Prasanna Deshapriya, E. A. Cloutis, B. E. Clark, A. R. Hendrix, A. Sen, M. M. Al Asad, M. G. Daly, D. M. Applin, C. Avdellidou, M. A. Barucci, K. J. Becker, C. A. Bennett, W. F. Bottke, J. I. Brodbeck, H. C. Connolly Jr., M. Delbo, J. de Leon, C. Y. Drouet d'Aubigny, K. L. Edmundson, S. Fornasier, V. E. Hamilton, P. H. Hasselmann, C. W. Hergenrother, E. S. Howell, E. R. Jawin, H. H. Kaplan, L. Le Corre, L. F. Lim, J. Y. Li, P. Michel, J. L. Molaro, M. C. Nolan, J. Nolau, M. Pajola, A. Parkinson, M. Popescu, N. A. Porter, B. Rizk, J. L. Rizos, A. J. Ryan, B. Rozitis, N. K. Shultz, A. A. Simon, D. Trang, R. B. Van Auken, C. W. V. Wolner, D. S. Lauretta

*Corresponding author. Email: danidg@lpl.arizona.edu

Published 8 October 2020 on *Science* First Release
DOI: 10.1126/science.abc3660

This PDF file includes:

Materials and Methods
Figs. S1 to S16
Tables S1 and S2
Captions for Data S1 to S3
References

Other Supplementary Materials for this manuscript includes the following:
(available at science.sciencemag.org/cgi/content/full/science.abc3660/DC1)

Data S1 and S2 (.xlsx)
Data S3 (.txt)

Materials and Methods

1. Image acquisition and calibration

PolyCam images were acquired under varying imaging conditions in the Detailed Survey mission phase (*1,25*), and MapCam images were collected on 14 March 2019 (Baseball Diamond Flyby 2) and 26 September 2019 (Baseball Diamond Flyby 2b). OCAMS images were radiometrically calibrated, corrected for charge smear, and converted into units of reflectance (*I/F* or radiance factor) using previously described techniques (*29*). Calibrated OCAMS data have a 5% absolute radiometric uncertainty and a 1% relative uncertainty (*29*). PolyCam images were used only for geologic context so were not photometrically corrected. MapCam images were photometrically corrected to solar phase (α), incidence (i), and emission (e) angles of 0°. Correcting (i, e, α) to 0°,0°,0° converts the reflectance data into a measure of normal reflectance (*73*). Photometric correction used a Lommel-Seeliger disk function and the Robotic Lunar Observatory (ROLO) phase function (*30*). The ROLO model is preferred for correction to 0° phase because it accounts for Bennu's small opposition surge (*30*), which is slightly stronger in the *b′* band (versus the other photometric filters). The accuracy of the correction is dominated by the accuracy of the global 3D tessellated digital terrain model (DTM) used to calculate the photometric angles and the registration of the images to that shape model. We used an OLA-based shape model (v20) with a 20 cm facet size for photometric correction (*36*).

2. Image mosaicking and photogrammetric control

Image mosaicking was performed using a version of ISIS3 (*74*) modified to support processing with tessellated 3D shape models. Precise co-alignment between different filter images is imperative for spectral analysis. It is assumed that color images are acquired in sets where each filter is taken in some consecutive order and as close in time as possible. To achieve color registration of MapCam images, the photogrammetric control process is performed in two stages.

The first stage is focused on spatial registration between overlapping images and accurate alignment with a DTM; we used the 80 cm mean facet size v28 shape model of Bennu by updating the existing model (*6*) using stereophotoclinometric techniques. The initial image control network was created with a single MapCam filter and exposure time; we used the *v* band (0.55 μm) at the longest exposure time (18.29 ms). Long exposures have the highest single-to-noise ratio for images of Bennu's dark surface materials but can saturate very bright features. We discarded saturated pixels in our analysis. The photogrammetric control process involved global registration of all *v* band filter images, and used OCAMS image mosaicking procedures described elsewhere (*25, 32*). The adjusted camera pointing for each individual *v* band image after bundle adjustment resulted in an improvement in the registration between overlapping images and the registration between images and the modeled terrain of Bennu. The improvement was evaluated by creating a basemap with the corrected *v* band images and comparing it with a shaded relief of the DTM.

The second stage involved creating individual color sets by pairing each corrected *v* band image with a corresponding remaining filter acquired close in time. The photogrammetric control procedure involves adjusting the camera pointing of the remaining filters within a color set directly to the corresponding newly adjusted *v* band image. This process ensures that the camera pointing

of each remaining filter image matches that of the *v* band. The end results are maps in each MapCam band (*b′, v, w, x*) and span 0–360° longitude and ±65° latitude.

To create color cubes, we performed subpixel image-to-ground and image-to-image registrations. The *b′/v* ratio (0.47 μm/0.55 μm) represents the near-UV index. The *x/v* ratio (0.86 μm/0.55 μm) represents the mid-VIS to NIR slope. We also calculated the relative band depth of the *v* (0.55 μm) and *w* (0.7 μm) bands using an equation for relative band depth (*2*). Band ratio maps were normalized against Bennu's median global values, and therefore emphasize variation from the average. We applied a 7 × 7 boxcar lowpass filter combination to reduce speckle noise in the band ratio cubes. Stray light was also reduced using a cube-to-cube normalization procedure for the *w* (0.7 μm) relative band map.

3. Principal component analysis of color mosaics

We performed a principle component analysis (PCA) on the color data to identify the maximum variance of spectra from Bennu. We used MATLAB's built-in PCA functionality (*75*), which returns the principle component (PC) scores for each pixel, mapped into the first, second, and third components. Subsequently, we identified spectral features by selecting portions of the histogram of each PC and calculating the average spectrum of the pixels that fell within the high and low ranges of the PC, as determined by examining geologic features (figs. S1 to S3).

Before performing PCA, we applied a Gaussian filter (2 pixel kernel width) to the individual color bands to mitigate singe-pixel noise. We removed shadows from the maps such that spectral variations within those shadows did not influence the PCA. To remove shadows, we set all pixels with an albedo less than 0.03 to null. Any pixel removed from a single band was removed from all bands. The first principal component (PC1) shows a wide range in albedo, whereas the second (PC2) discriminates changes in the overall spectral slope (from *b′* to *x*), and PC3 indicates variation in the near-ultraviolet (from *b′* to *v*) (figs. S1 to S3). PC4 is the noise floor and reveals the areas where scattered light and incomplete smear correction impact the data at a scale of about 0.5%. The eigenvalues and statistics obtained from the PCA performed on the four MapCam bands is given in table S1.

4. Mapping and classifying geologic features on Bennu

Boulders were mapped with polygons in ARCMAP on Bennu's MapCam color mosaics. The dataset includes 1590 boulders and we consider it a complete, representative population down to 13.55 ± 2.35 m in diameter, although many boulders as small as 1.5 m were also included in this analysis. Separate boulder populations have previously been identified based on albedo, but did not have sufficiently well-constrained photometry to assess their distributions (*4*).

We determined that the histogram of the MapCam *v* band normal reflectance observed for each boulder (Fig. 2A) has a multi-modal distribution by testing whether the data were normally distributed using the Anderson-Darling test, and subsequently using the MCLUST routine in R (*76*) to determine the number of Gaussian components present in the distribution. These tests indicate 99% confidence that the boulder reflectance data presented are not drawn from a population having a single normal distribution. The MCLUST routine identified a 4-component Gaussian mixture as the best fitting model of the data, although any multi-modal distribution is a better fit than a

unimodal one. The mean *v* band reflectance and standard deviations of the 4-component model are 0.0412 ± 0.003, 0.0447 ± 0.002, 0.0551 ± 0.004, and 0.075 ± 0.020, and the number of boulders falling into each component are 341, 621, 619, and 10. These values indicate that the dark boulders may comprise two separate populations, or that our thresholding procedures to remove shadows are influencing the spectrophotometric statistics of the lowest-reflectance surfaces.

We distinguished between the low- and high-reflectance boulder populations by thresholding at a *v* band reflectance value of 0.049, which is the median between the two visible peaks of the boulder reflectance distribution. Based on the presence of composition indicators, we classified boulders into Fe-bearing phyllosilicate or pyroxene-bearing boulders on the basis of their *w*-band strength $wbs = w / (0.5v + 0.5x)$, using the median *wbs* value ±3 times the median absolute deviation (MAD) for thresholding. The MAD is a standard statistical method of measuring dispersion and identifying outliers. Fe-bearing phyllosilicate boulders had low *wbs* values (less than $\mathrm{median}(wbs) - 3\mathrm{MAD}(wbs)$), signifying an absorption at 0.7 μm. Pyroxene-bearing boulders had high *wbs* values (greater than $\mathrm{median}(wbs) + 3MAD(wbs)$), signifying an absorption longward of 0.85 μm and a negative b' to *v* reflectance slope. We manually inspected boulders that were close to the classification boundaries to confirm their classification. The four distributions identified by MCLUST have similar mean *v*-band reflectance values to those from the boulder categories identified in this manual classification. The agreement between the different techniques applied improves our confidence that multiple populations of boulder types are present on Bennu.

For the calculations of the b' to *x* spectral slope for boulders and craters, we adapted an equation (*77*) for the MapCam bands:

$$\bar{R}_i = 1 + \gamma(\lambda_i - 0.55\mu m) \qquad \text{eq. S1}$$

where R_i is the reflectance in each band (b', *v*, *w*, *x*) normalized to the *v* band, λ_i is the effective wavelength (in microns) of each band (0.473, 0.550, 0.698, 0.847), and γ is the slope of the fitted line, constrained to a value of unity at 0.55 μm.

We determined the relationship between reflectance and the b' to *x* spectral slope by first conducting an Anderson-Darling normality test for both variables, which indicated ≫99% confidence that neither variable is normally distributed. We therefore conducted a non-parametric correlation test, Kendall's Tau. For Kendall's Tau, as with other correlation metrics, $-1 \leq \tau \leq 1$, and $\tau = 0$ when variables are independent. We found significant evidence ($p \ll 0.01$) to reject the null hypothesis and conclude that dark boulder reflectance and spectral slope have a moderate, monotonically decreasing relationship ($\tau = -0.43$). We conducted the same tests for the bright boulders, among which boulder reflectance and spectral slope have a weaker monotonically decreasing relationship ($p \ll 0.01$, $\tau = -0.29$).

Crater identification within ± 60° latitude was performed using panchromatic PolyCam image data (not MapCam color images) acquired during the Approach and Detailed Survey phases of the OSIRIS-REx mission (*1,25*). The Approach images provide global coverage at approximately ~30 cm pixel^{-1} and are suitable for identifying and measuring craters with diameters larger than ~30 m (*33*). The Detailed Survey images provide complete coverage of the surface in latitudes ±60° at low emission angles and with an average of ~5 cm pixel^{-1} (*32*), and permit identification and measurement of craters to diameters <1 m. Images were displayed over Bennu's shape model

using the SMALL BODY MAPPING TOOL (SMBT (*78*)), which provides continuously adjustable zoom levels, brightness/contrast control, and manipulation of viewing direction of the shape model. Such manipulation allowed us to set different image parameters to search for features of all scales and brightness levels within the images. Craters were identified by morphology characteristics, primarily via circular depressions, sometimes with particle-size contrasts between the crater interior and exterior. Craters were marked using SMBT's circle or ellipse tool, which records the location and geometry of the circle or ellipse in the coordinate system of the shape model. We subsequently confirmed that >90% of the craters identified in PolyCam images have morphological expression in the OLA data (*36*).

The crater database of sizes and locations was then correlated with the color data set to identify color trends of the craters. Craters were manually registered with Bennu's global color mosaics in ARCMAP. We also debiased the color statistics of overlapping craters, by only using the surface area (pixels) belonging to each crater to calculate statistics. We assume smaller craters were created more recently, thus large craters with overlapping small craters were clipped to remove the shared pixels that belonged to smaller craters. The dataset includes 706 craters; we consider it to be a complete population down to 3.10 ± 0.4 m in diameter, following (*4*). The power law index of the crater size frequency distributions was determined using the methods described in (*4*) for boulder distributions.

5. Analysis of the crater colors, size-frequency distribution, and production function

The absolute spectral slope from the b' to x bands was calculated for the global list of craters. The values for each were then compared directly to the global Bennu average surface b' to x slope (–0.1701 with standard deviation 0.1003). Craters were extracted from the list based on their measured color relative to the global color. The subset of craters that were 1σ redder than average had b' to x slopes greater than –0.0701 (a total of 79 craters met this criterion, and only three were more than 2σ redder). The 255 craters that were 0.5σ redder than average were also extracted.

We determined the relationship between crater reflectance and the b' to x spectral slope by first conducting an Anderson-Darling normality test for both variables, indicating ≫99% confidence that neither variable is normally distributed. Kendall's Tau test indicated significant evidence ($p \ll 0.01$) to reject the null hypothesis and conclude that crater reflectance and spectral slope have a moderate, monotonically decreasing relationship ($\tau = -0.54$).

The differences in the b'/v band ratio of craters categorized by their overall b' to x spectral slope (Fig. 6) were statistically assessed using a one-way analysis of variance (ANOVA). To perform this test, we assumed that the b' to x spectral slope is dominated by the change from v to x and is thus independent from the b'/v band ratio; the spectral changes in Figure 5 support this assumption. The results, summarized in table S2, demonstrate that the F value, F, is larger than the F statistic, F_{crit}, and so we can reject the null hypothesis. Additionally, the mean and median of each category indicate steeper b'/v band ratios for intermediate b' to x spectral slopes; that is, craters with the most positive and negative b' to x spectral slopes are less blue in the near-UV.

The crater production function is a combination of the expected flux of impactors for a near-Earth object, their typical impact speeds, and the crater scaling expected for impacts into a small rubble-

pile asteroid. The flux of impactors in the size range of 1 to 10 m has been measured via bolide detonations in Earth's atmosphere (*47*). The power-law size distributions of these impactors match that for larger bodies (*48*) and are combined to produce an expected flux of impactors per year per square kilometer of a near-Earth asteroid.

We used the gravity-regime crater scaling relationship (*50,51*), incorporating the surface gravity of Bennu (0.0000615 m s^{-2} (*6*)) and a typical target grain size of 30 cm. Impactor density was assumed to be 2300 kg m^{-3}, target bulk density was assumed to be that measured for Bennu of 1190 kg m^{-3} (*6*), target grain density was assumed to be 2300 kg m^{-3}, solid target disruption energy was assumed to be 1000 J/kg, and an impact speed of 18.5 km s^{-1} was used to represent the mean impact speeds between near-Earth asteroids (*79*).

6. Calculating spectral slopes across individual dark boulders

We examined nadir MapCam images taken during the re-fly of Baseball Diamond Flyby 2 (26 September 2019) and identified 220 large boulders between ±20° in latitude (boulders outside of this latitude range were imaged with emission angles >20°). The rim of each boulder was manually traced in MapCam images. Based on the manually traced boulder outline, we calculated the azimuthal angle that maximizes the blue-to-red color variation within each boulder. We calculated the difference in the average b' to x spectral slope between the two regions within the outline of each boulder, which is divided by a line segment with a variable angle crossing the centroid of a boulder. Pixels with incidence/emission angles > 60° and $I/F < 0.01$ were discarded from the calculation. The optimal angle was identified via a grid-search between 0° to 360° range with 30° intervals in each boulder image. The determined angles were converted to azimuthal angles shown in fig. S11 by georeferencing the images to an equirectangular projection.

Fig. S12 shows intra-boulder variation. Whether such color variation could be a product of the illumination conditions (e.g., inclusion of sub-pixel scale shadows) was evaluated by calculating the root mean square (RMS) error of the radiance factor using multiple images taken with slightly different viewing angles during the flyby sequence. The distribution of the RMS deviation showed limited correlation with the observed intra-boulder color variation; thus, the observed variation should at least partly reflect the surface property of boulders.

7. Spectrophotometric trends and comparison between Bennu and Ryugu

The *I/F* distribution (fig. S13) was calculated by using the global observation images: PolyCam images of Bennu taking during the OSIRIS-REx mission's Approach and Preliminary Survey phase (20181113T041412S224_pol_iofL2pan to 20181113T083212S153_pol_iofL2pan) and ONC-T (Optical Navigation Camera) *v* band images of Ryugu taken during the Hayabusa2 mission's Box-A Operation (hyb2_onc_20180712_064513_tvf_l2d to hyb2_onc_20180712_134452_tvf_l2d). These images were chosen due to their similarity in resolution (~2 m $pixel^{-1}$) and phase angle (18–19°), minimizing observational biases between the OCAMS and ONC data sets. To account for the different shapes of the two asteroids, the *I/F* values were photometrically corrected to an observation geometric condition (i, e, α) = (18°, 0°, 18°). Similar-resolution shape models (~3 m facets) were used for the correction (stereophotoclinometry v20 (*6*) for Bennu and stereophotoclinometry v20180717 for Ryugu). The photometric functions

and parameters were taken from the fitting conducted by using images taken under a wide range of conditions (*30, 68*). Pixels with incidence or emission angles >60° and $I/F < 0.01$ were discarded because of the uncertainties in the photometric correction and their low signal-to-noise.

I/F pixels were mapped to an equirectangular projection. Each mesh in the equirectangular projection was weighted with a cosine of latitudes to account for the areal distortion to create the areal frequency histogram. Each histogram was normalized by its total area. The photometrically corrected images were binned in 32 × 32 pixel bins to calculate the distribution at a pixel scale of ~64 m.

The same method was applied to the color distributions (fig. S13). We used color images from MapCam during the OSIRIS-REx Baseball Diamond Flyby 2b for Bennu and ONC-T the Box-A Operation for Ryugu (*68*). The difference in the resolution was compensated for by conducting an 8 × 8 pixel binning of the MapCam images.

For the comparison between Bennu and Ryugu, the b' to x spectral slope was calculated as:

$$\frac{b'/v - x/v}{\lambda_{b'} - \lambda_x} \qquad \text{eq. S2}$$

The effective wavelengths are slightly different with the MapCam and ONC-T filters ($\lambda_b = 0.4798$ μm, $\lambda_v = 0.5489$ μm, and $\lambda_x = 0.8573$ μm for ONC-T (*80*)). This effect was quantified by calculating the difference in band ratios of the 398 C-complex asteroids surveyed by Small Main-Belt Asteroid Spectroscopic Survey, Phase II (SMASS2) (*77*) using the respective wavelengths of the two cameras. The difference in the band ratios was confirmed to be ~1% (RMS error of 1.1 % for b'/v and 0.99% for x/v) and thus would not affect our qualitative results.

A Student's t-test was used to assess the significance of the difference between the means of Gaussian-like equatorial and mid-latitude color distributions on Bennu (fig. S13D). The means for Ryugu and Bennu are significantly different with $p \ll 0.01$. This trend holds after the photometric correction (*30*) ($p \ll 0.01$). Thus, the slight bluing of Bennu's equator relative to the mid-latitude regions is likely not due to observational biases.

8. Spectral Analogs of Bennu

Although carbonaceous meteorites are expected to be a reasonable compositional analog for Bennu, the reflectance of Bennu is lower than that of most meteorite samples. To reproduce the spectral reflectance properties and variations seen on Bennu, we produced a series of physical and simulated analogs consisting of two-component mixtures of an Mg-rich phyllosilicate, saponite, magnetite and one of two forms of carbon, graphite or lampblack (shown in fig. S4 C and D).

Simulated analogs (fig. S4 D) used the samples and procedures outlined in (*44*). For physical analogs, we produced a series of them spanning a range of carbonaceous material abundances (0–10 wt.%). We used saponite (containing ~25 wt.% dolomite) as the primary phyllosilicate because Bennu may have been extensively aqueously altered, and as aqueous alteration proceeds, the abundance of saponite to serpentine in carbonaceous chondrites increases, and the phyllosilicates become increasingly Mg-rich (e.g., *81–84*). Because it is not possible to extract enough

carbonaceous material from carbonaceous chondrites to produce sufficient quantities of simulants, we used fine-grained amorphous carbon or graphite because it is not possible to extract enough carbonaceous material from chondrites to produce sufficient quantities of simulants. The amorphous carbon (lampblack) and graphite are spectrally featureless in the 0.3–5 μm region (*85*), and both induce a bluing (reflectance decreasing toward longer wavelengths) in mixtures with phyllosilicates (*86, 87*), (fig. S4C).

The series of saponite+lampblack and saponite+graphite mixtures that we produced have carbonaceous phase abundances that encompass (and exceed) the range of carbonaceous phase abundances in carbonaceous chondrites of types CI1 and CM1-2 (*88*).

Samples used: Our mixtures included a natural (but partially processed by the supplier) saponite (our sample #SAP105), a fine-grained synthetic lampblack (our sample #LCA101), and a synthetic graphite (our sample #GRP102). Sample sources were:

- SAP105 is sourced from Amargosa Valley, CA-NV, USA. It was provided as a fine-grained beige powder by IMV Minerals (Lhoist North America) and is marketed under the trade name Imvite.
- LCA101: Johnson Matthey, #14237A, <0.021 μm particle size. GRP102: Johnson Matthey, #10130A, –300 mesh, 99.5% pure.

Preparation of mixtures: To produce samples with intimately mixed phyllosilicates and opaques, we adapted a procedure developed (*89*) for Bennu analogs.

The as-received endmembers were all fine-grained (<45 μm), so no additional sample preparation was required. Mixtures were prepared by weighing out endmembers using a balance with an accuracy of ±0.1 mg. Approximately 50 grams of each mixture were produced. Each mixture was placed into an alumina mortar and pestle and ground together for one minute to remove clumping. The powders were then mixed with reverse osmosis (RO) water at a volumetric ratio of roughly 2:1 water:powder in a stainless steel cup with agitators. The resulting slurries were further blended with a commercial-grade drink mixer for roughly 10 minutes and then poured into aluminum trays with crenulated bottoms. The mixtures were then heated to 150°C in air and kept at that temperature for 4 days using a drying oven. The slurries were initially ~10 cm thick, and the heating process resulted in a very large volume loss and formation of mostly few-centimeter chunks due to desiccation cracking about 1 cm deep. The resulting chunks had a smooth cuspate surface with a surface coating of light-colored precipitate (likely halite), and a few vesicles (up to ~3 mm in diameter). The upper surfaces of the chunks were scraped with a razor blade to remove the salt crust. A portion of the sample was retained as-is, with the upper surfaces additionally sanded with 60 grit aluminum oxide sandpaper to produce a matte surface. Other portions of the sample were ground by hand in the alumina mortar and pestle and dry-sieved to produce <1000 and <45 μm powders, also after removing the salt crusts. This resulted in four different types of samples for spectral analysis: flat-matte surfaces, crenulated surfaces, <1000 μm powders, and <45 μm powders.

Scanning electron and optical microscopy indicated that the lampblack was not fully dispersed in the mixtures. The samples showed some areas of clumped lampblack with the larger aggregates about 30–50 μm in diameter. Carbon and carbonaceous material mapping of CM chondrites shows

that carbon-rich domains range in size from <1 μm to a few to tens of microns and are heterogeneously distributed (e.g., *90,91*), so that incomplete disaggregation of the lampblack more closely reproduces carbonaceous chondrite matrix textures than complete disaggregation would.

Supplementary Figures

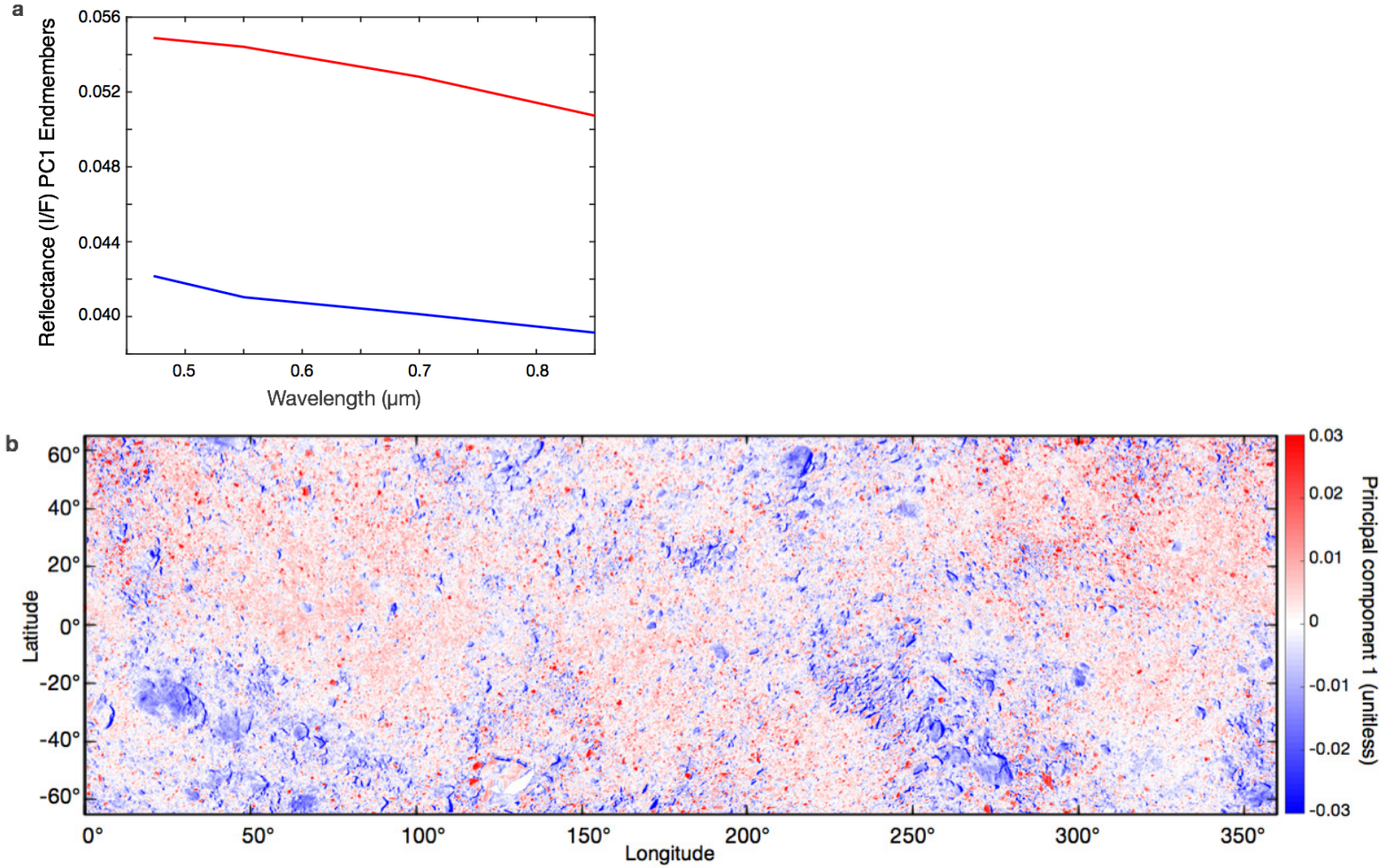

Fig. S1. Principal Component 1. (**A**) The average spectra for the high and low endmembers of the histogram of PC1. (**B**) PC1 mapped across the surface of Bennu. The red and blue spectra correspond with high and low values in the map of PC1, respectively. The overall change in albedos across Bennu is captured by PC1, which tracks with the *v* band normal reflectance.

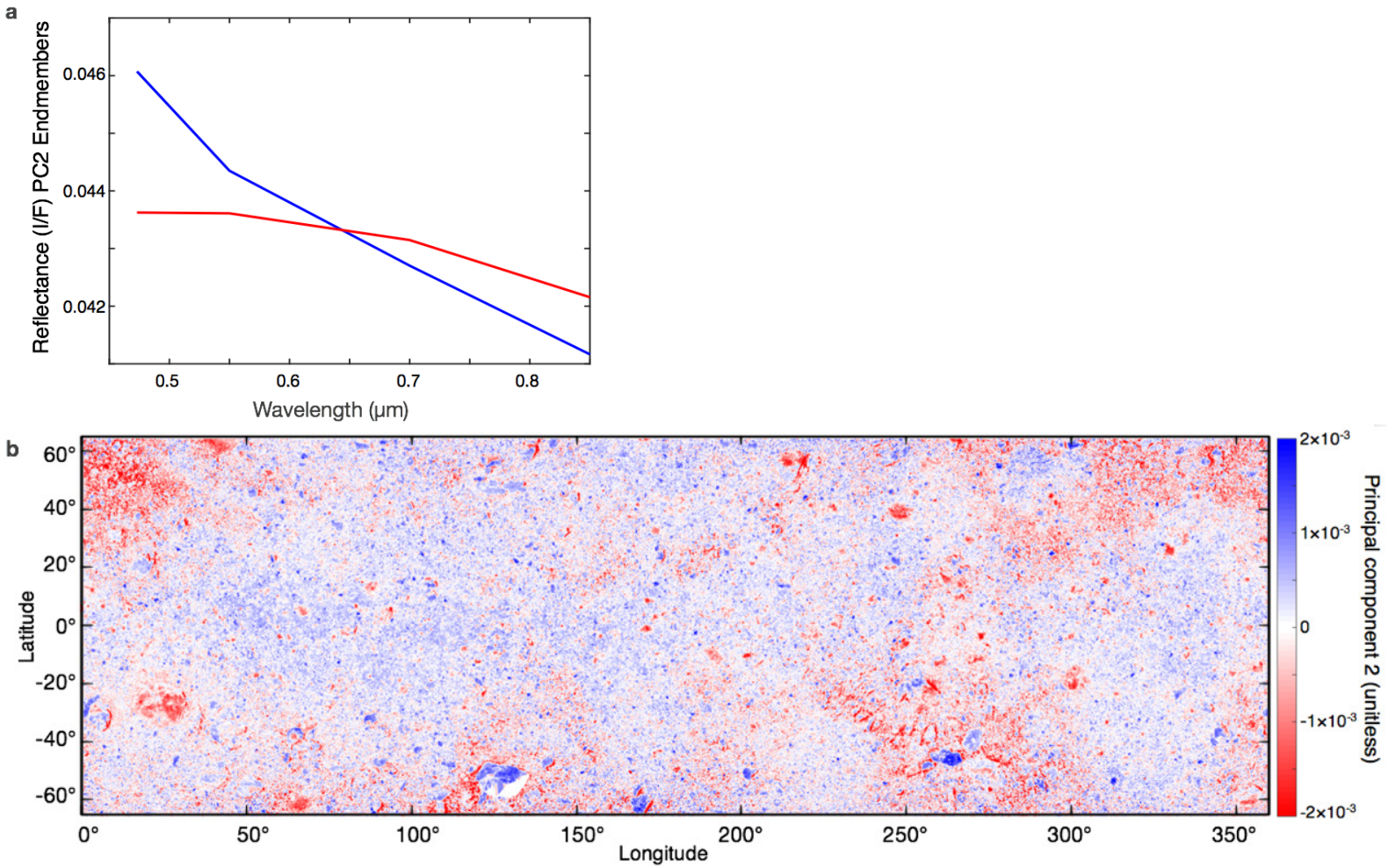

Fig. S2. Principal Component 2. (**A** and **B**) Same as in fig. S1, but for PC2. The overall spectral slope (from b' to x) appears to drive the variance of PC2 and tracks the b'/x band ratio.

5

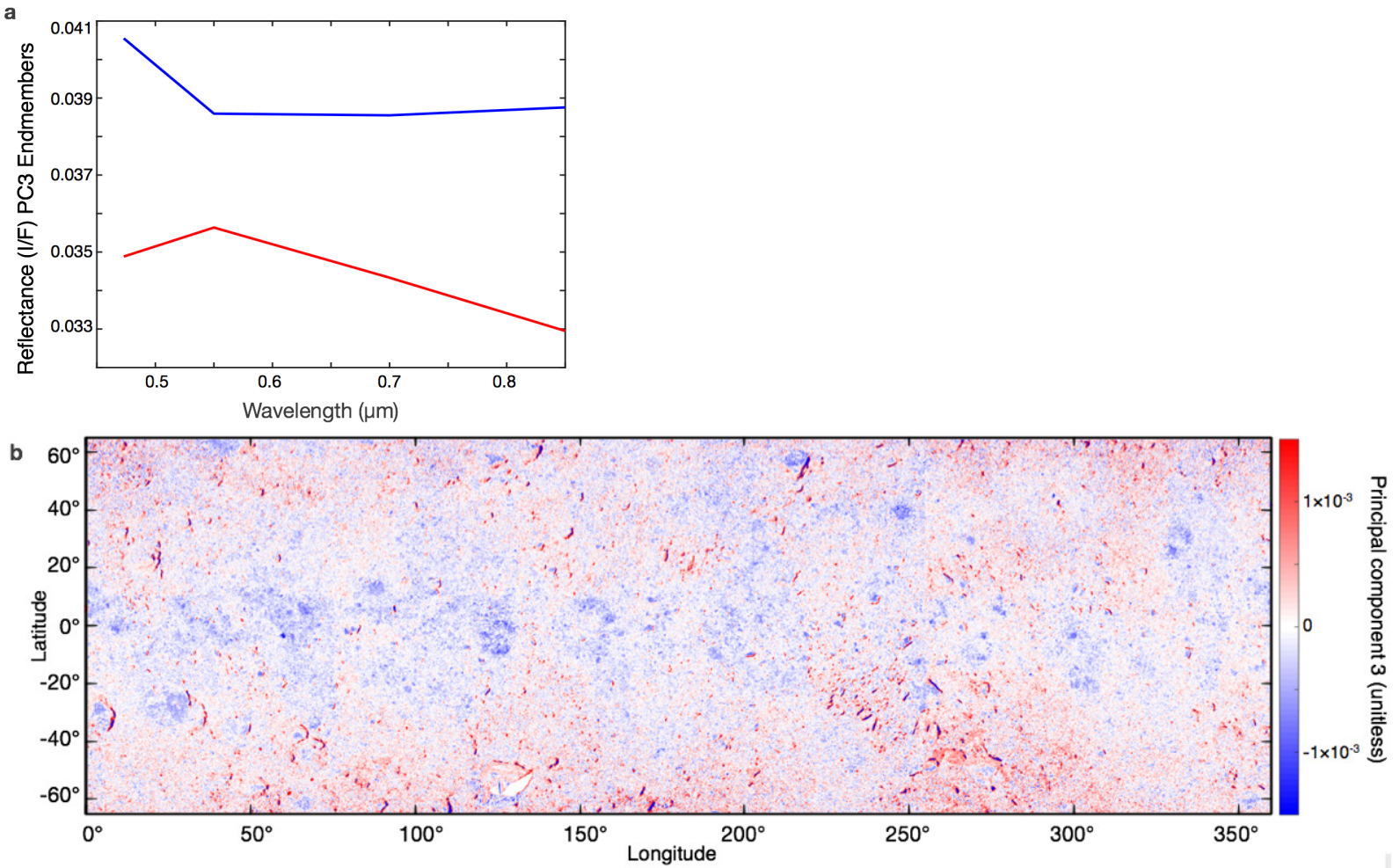

Fig. S3. Principal Component 3. (**A** and **B**) Same as in fig. S1, but for PC3. Most spectral variance in PC3 corresponds to an upturn or downturn in the *b′* band and tracks the *b′/v* band ratio.

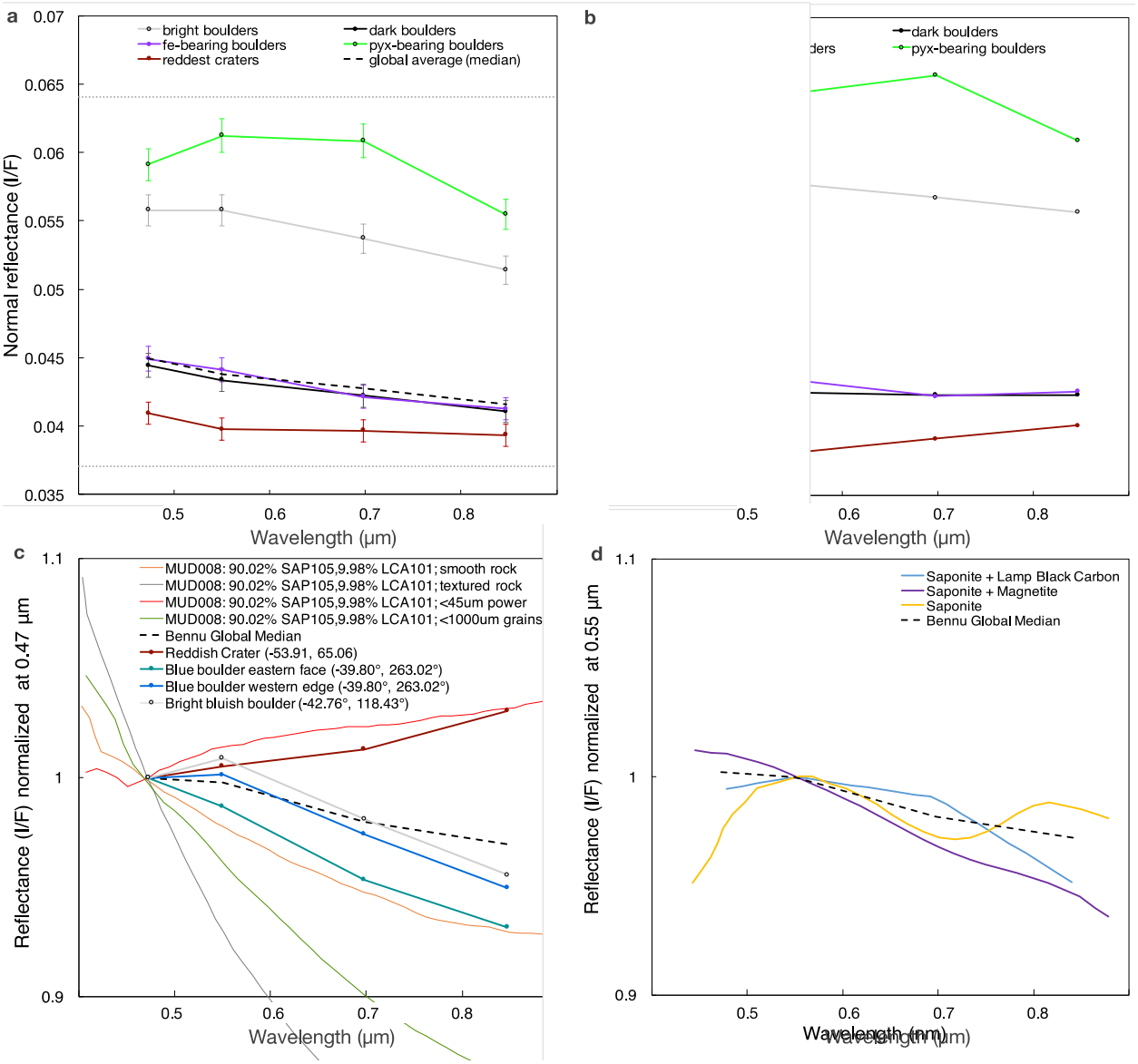

Fig. S4. Reflectance of boulders, craters, and Bennu analogs. (**A**) Average (median) spectra in absolute normal reflectance of each color unit identified in Table 1. Error bars represent that 2% relative radiometric uncertainty in MapCam data and the light gray dotted lines encompass the 5% range of absolute radiometric uncertainty. (**B**) Same spectra shown in (A) ratioed with the global median spectrum of Bennu, which removes the relative and absolute uncertainties. (**C**) MapCam photometric spectra (solid circles connected by solid lines) for various color units as compared with Bennu's global spectrum (black dashed line) and laboratory samples (solid lines; labeled MUD008) of the phyllosilicate saponite (~90%) mixed with lampblack carbon (10%) and prepared in different textures. (**D**) The serpentine saponite combined, modeled in intimate mixtures with both magnetite and simulated fine-grained lampblack carbon. The models demonstrate the bluing effects of both magnetite and carbon (in this case, lampblack); the bluing effects are expected to vary depending on grain size, abundance, and "host" serpentine. Bennu's global spectrum (black dashed line) has a blue spectral slope that falls between both mixtures.

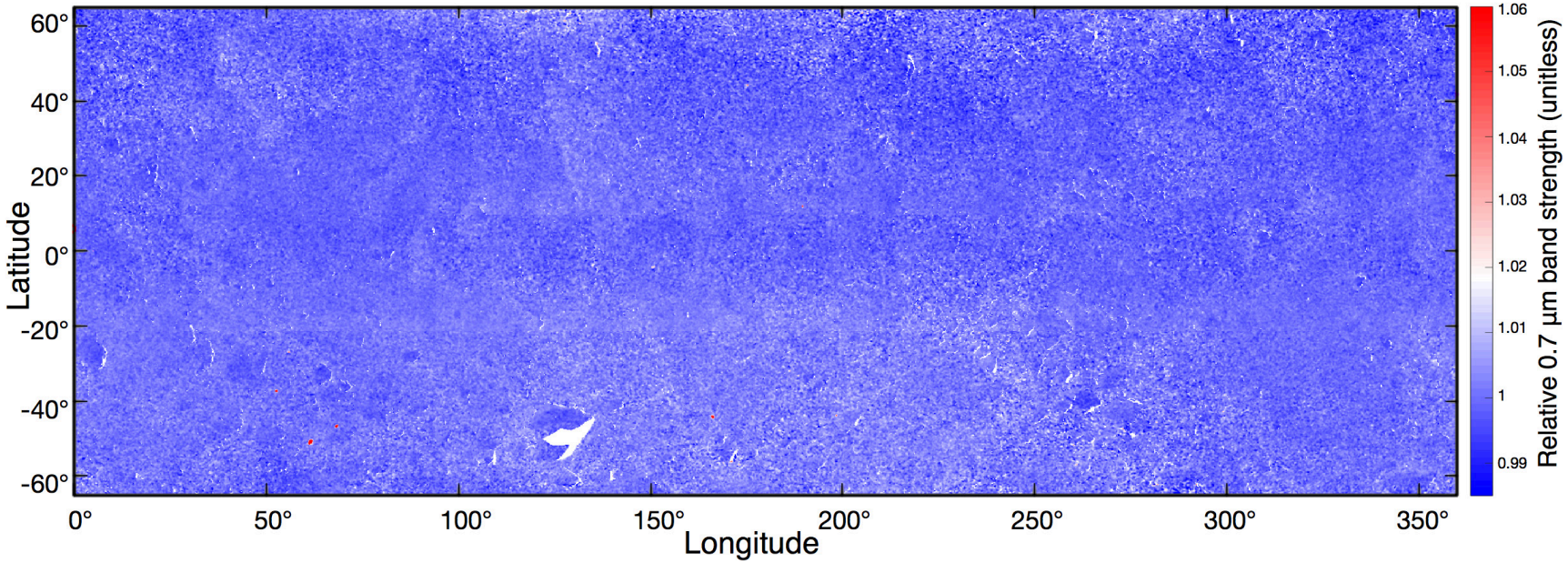

Fig. S5. MapCam mosaic (25 cm pixel^{-1}) of the relative band strength at 0.7 µm. Some larger dark boulders appear to have a weak (~1%) absorption feature (values <1). Although this weak absorption feature is at the radiometric precision of the MapCam instrument, its spatial coherence with individual boulders provides confidence that it is real. However, at the 1% level, minor artifacts, such as stray light (which causes linear artifacts at image seams), are also visible. Pyroxene-bearing boulders have band strengths at 0.7 µm >1 and appear as meter-scale red patches.

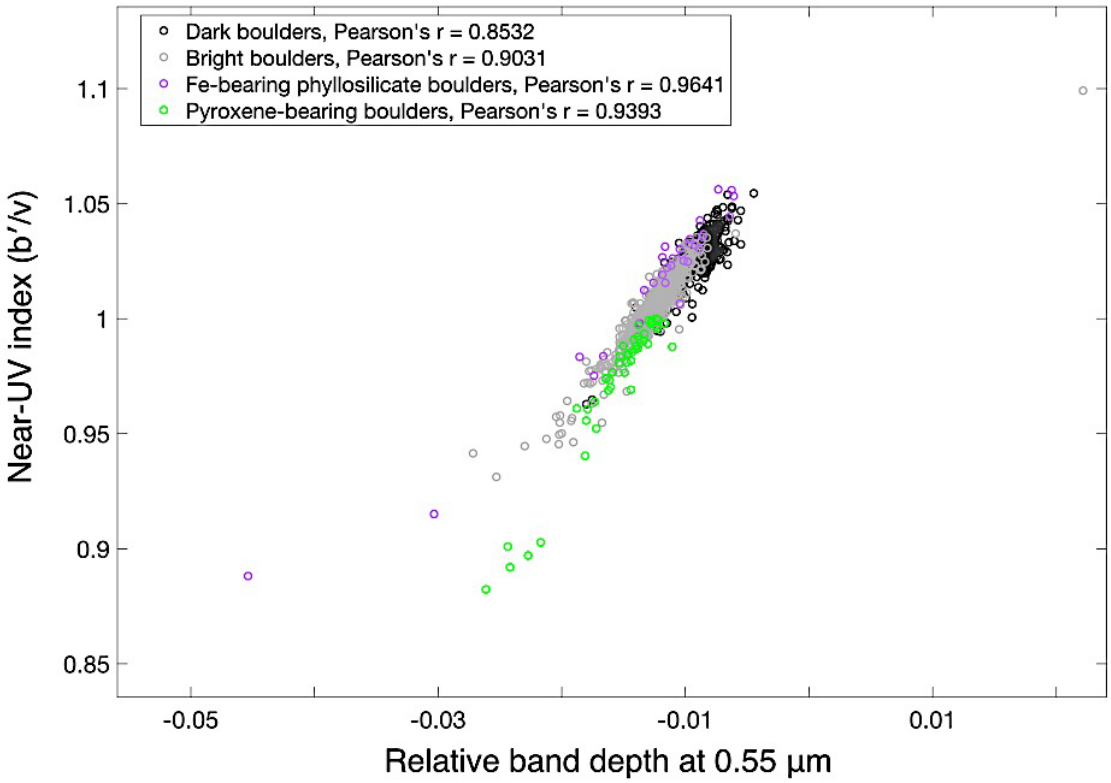

Fig. S6. The *b′/v* band ratio (near-UV index) as a function of the relative band depth at 0.55 µm for the different boulder types identified on Bennu. These quantities are linearly correlated for the different boulder types. The upturn in the near-UV observed in the spectra of some boulders may be the result of an absorption feature at 0.55 µm.

Fig. S7. PolyCam image (~5 cm pixel^{-1}) of the primary OSIRIS-REx sample site, Nightingale (white circle), acquired on 12 April 2019. This location appears smoother and is less well resolved than the bulk of the asteroid's surface. The texture of Nightingale is representative of many of the small reddish craters on Bennu. The image was taken from a distance of 2.8 km. The field of view is 39.6 m on each side.

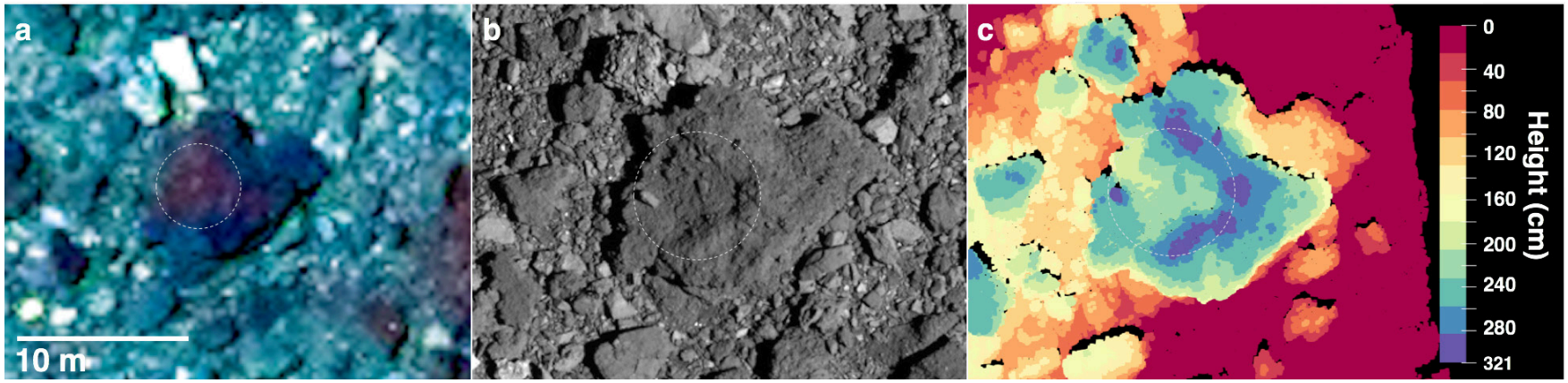

Fig. S8. Example of a crater on a boulder. (**A**) MapCam RGB false-color composite (same stretch as Fig. 3A) of a boulder with a putative crater (white dashed line), (**B**) as visible in a higher-resolution PolyCam image (5.25 cm pixel^{-1}), and (**C**) the local OLA DTM. The recessed crater in this boulder is spectrally redder than its surroundings.

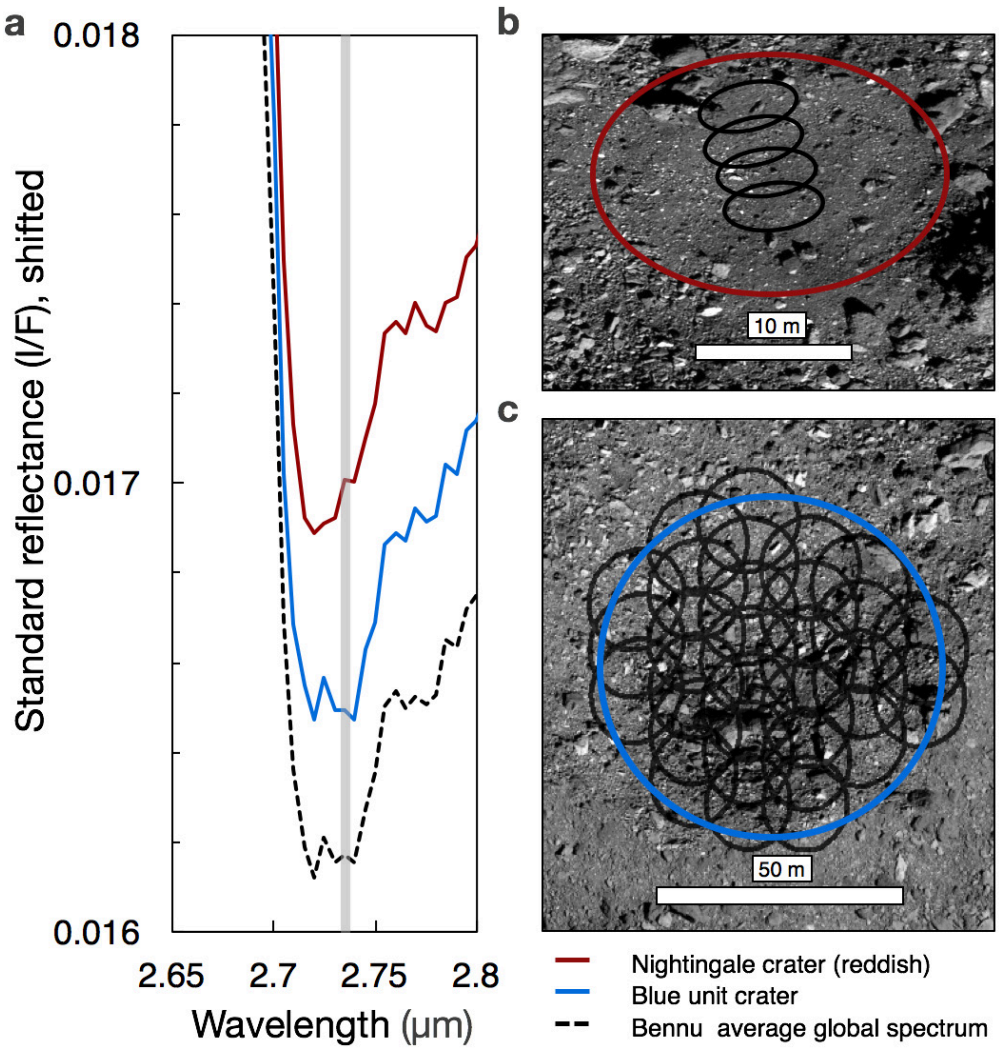

Fig. S9. (**A**) Non-normalized OVIRS spectra for Nightingale crater (solid red line), the blue unit crater at 1.06°lat, 152.75°lon (solid blue line), and Bennu's global average (dashed black line), corrected to standard reflectance conditions (30°, 0, 30°). The red and blue spectra are vertically shifted for display by –0.001 and –0.0033, respectively. The wavelength range was chosen to emphasize the minima of the 2.7-μm band associated with hydrated phyllosilicates. The gray vertical line indicates the minimum band position for the Bennu's global average, at 2.735 μm. For Nightingale crater, the band minimum is sharper, and its position is shifted (~15 nm) toward shorter wavelengths, compared to the global average. The blue unit crater's average spectrum has the same hydration band minimum as the global average at 2.735 μm. Still, the shape of the feature is sharper than that of the global average. The global average spectrum was obtained from all Detailed Survey OVIRS spectra (footprint size, 20 m) from the 12:30 PM local solar time Equatorial Station (09 May 2019). (**B**) Footprints of the four spectra of Nightingale averaged together for the red spectrum in (A). Data are from the Recon A phase of the mission (12 Oct. 2019), where the OVIRS footprints span ~6 m. (**C**) The footprints of the 28 individual spectra from 12:30 PM local solar time Equatorial Station were used to determine the blue spectrum in (A), which is bluer than the global average by a factor of ~3 in the range 0.55–2 μm (when normalized at 0.55 μm).

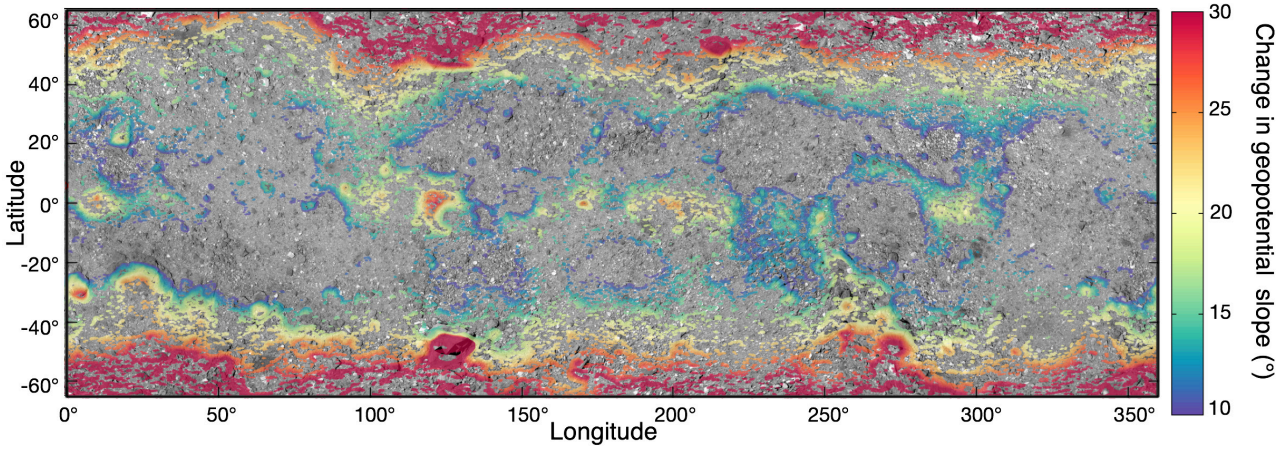

Fig. S10. The change in geopotential slope across the surface of Bennu as the spin period decreases from 5 hours to the present-day 4.3 hours over the past 200,000 years (*43*). The isolated region near 0°lat, 120–150°lon coincides with the presence of the equatorial blue crater units.

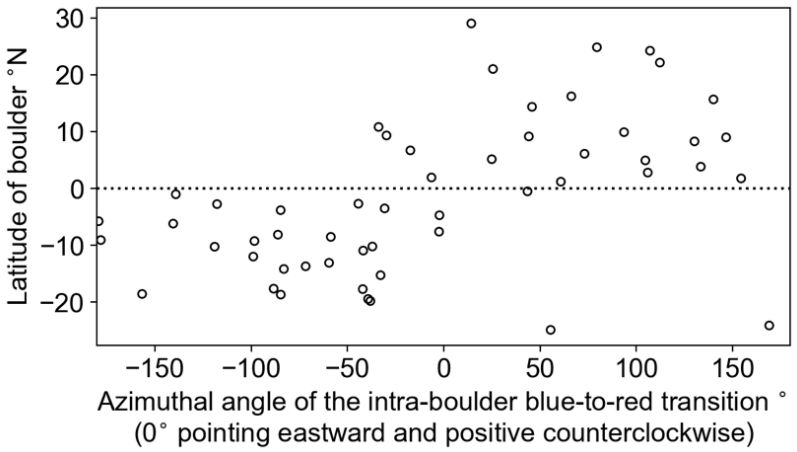

Fig. S11. Azimuthal angles of the intra-boulder color variation plotted against situated latitudes of boulders.

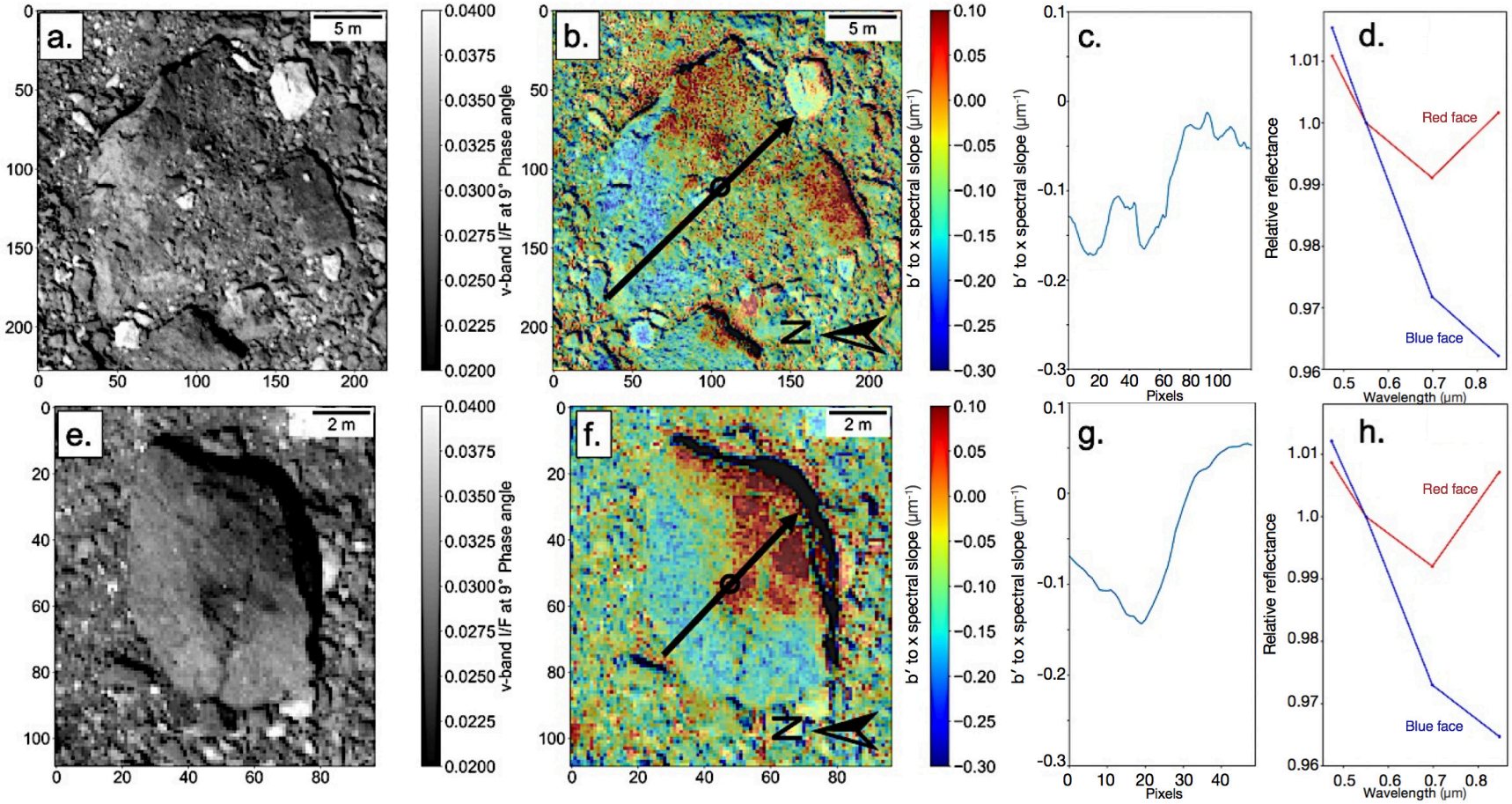

Fig. S12. Intra-boulder color distribution of boulders. (**A**) Image of a boulder situated at 20°S, 255°E (20190926T173725S586_map_iofL2v_V005.bvwx). (**B**) The *b′* to *x* spectral slope within the boulder. The arrow shows the calculated direction that maximizes the blue-to-red color variation. The circle indicates the centroid of the boulder. (**C**) The profile of the *b′* to *x* slope along the arrow shown in (B). The profile is smoothed by averaging over 20 pixels. (**D**) The *v* band normalized spectra of bluer and redder faces of the boulder. (**E** to **H**) Same as (A) to (D) for a boulder situated at 10°S, 260°E. Bluer surfaces tends to be brighter. The spectral difference between blue and red faces shows that the intra-boulder color variation is characterized by the heterogeneity in VIS spectral slope and the possible weakening of the 0.7-μm absorption, whereas the degree of UV upturn is relatively uniform.

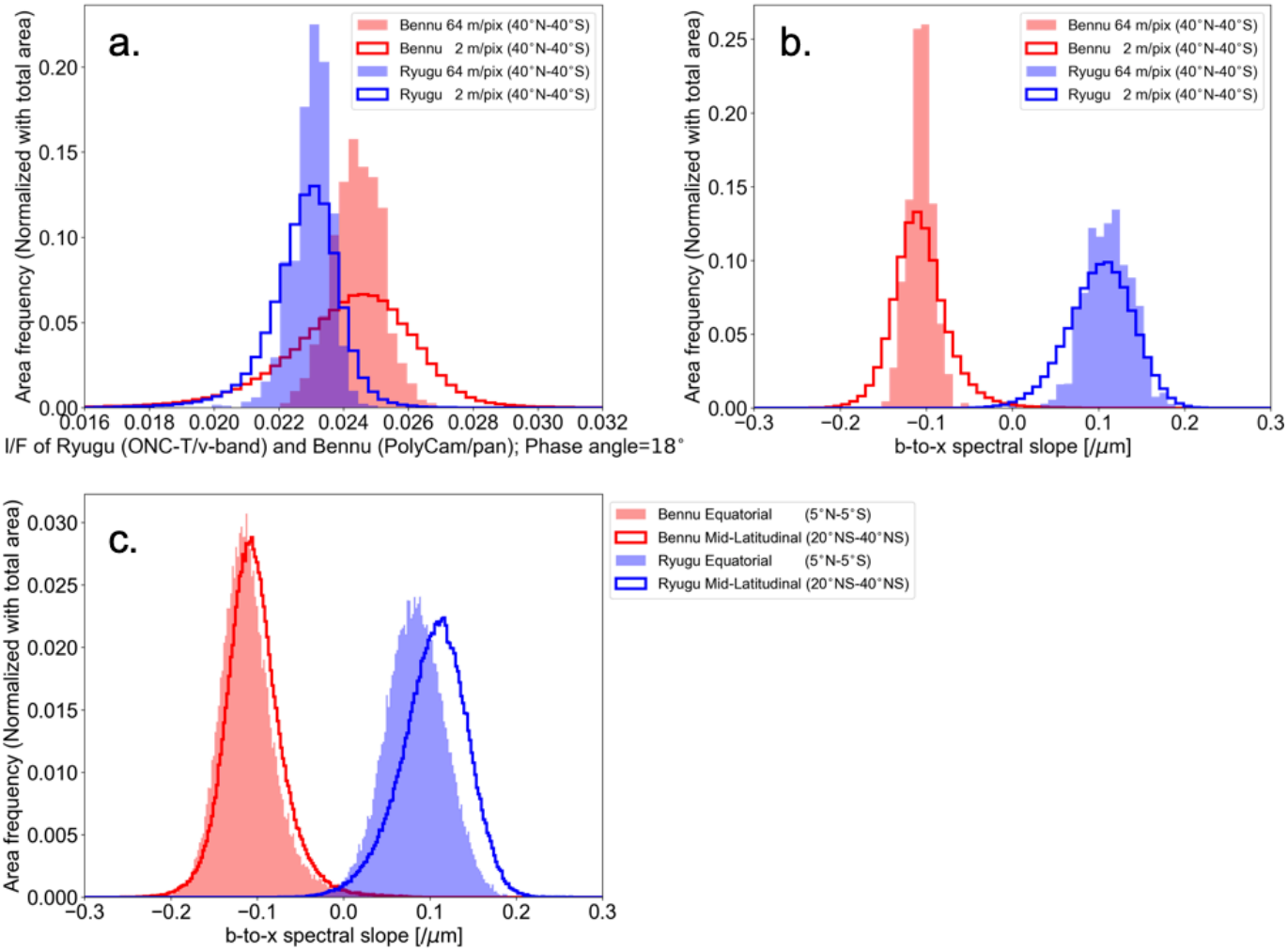

Fig S13. Comparison of the reflectance and color distribution between Bennu (red) and Ryugu (blue). The areal distribution of (**A**) reflectance and (**B**) spectral slope observed at ~2 × 2 m^2 and ~64 × 64 m^2 resolution. Owing to the slightly different effective wavelengths of the blue filters of OCAMS and ONC-T, spectral slopes are determined from *b* to *x* for Ryugu and *b′* to *x* for Bennu. (**C**) The change in the spectral slope distribution when averaged zonally at different latitudes.

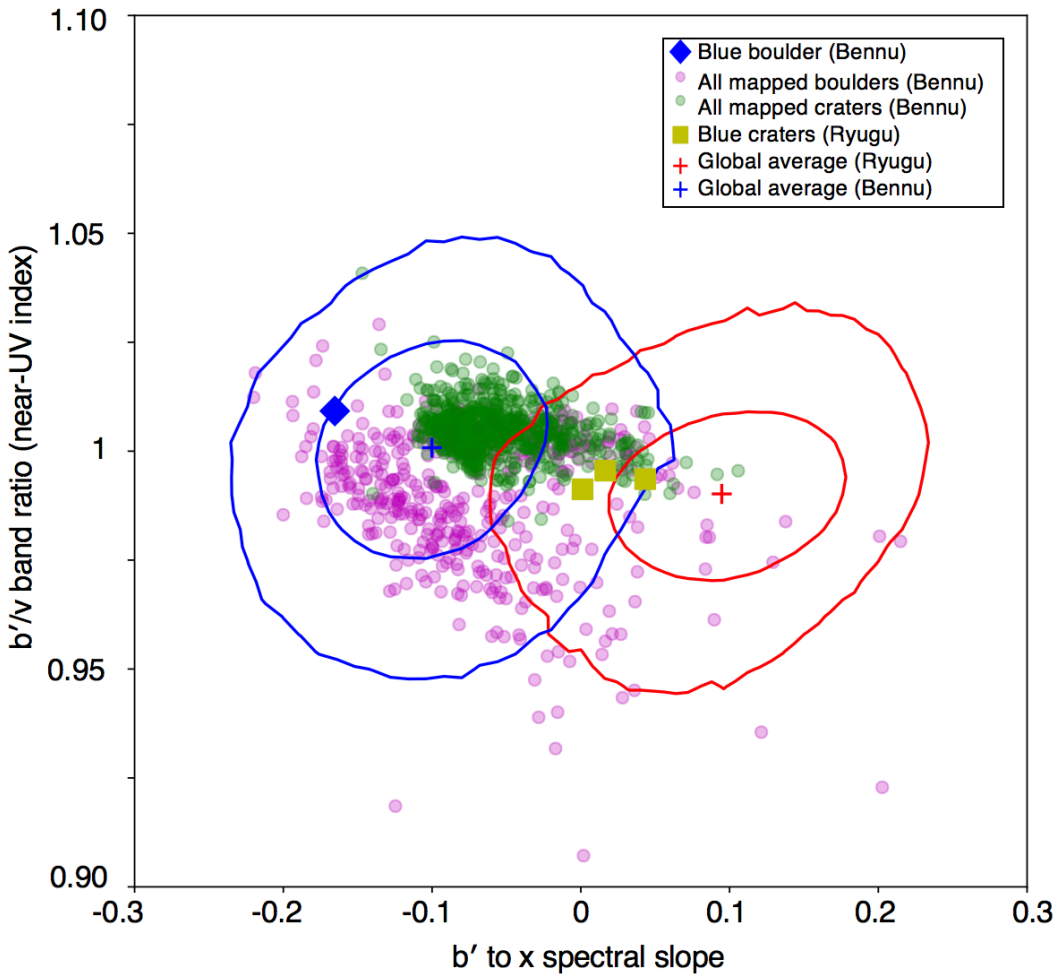

Fig S14. Comparison of Bennu's colors with the color of craters on Ryugu. The color of blue craters on Ryugu from (*70*) (yellow squares) compared to craters (green circles) and boulders (magenta circles) on Bennu. The *x* axis is the *b′* to *x* spectral slope, and the *y* axis is the *b′/v* band ratio (near-UV index). Bennu and Ryugu's average global values (crosses) are shown for context, with ellipses that indicate the variation for 68% and 95% coverage.

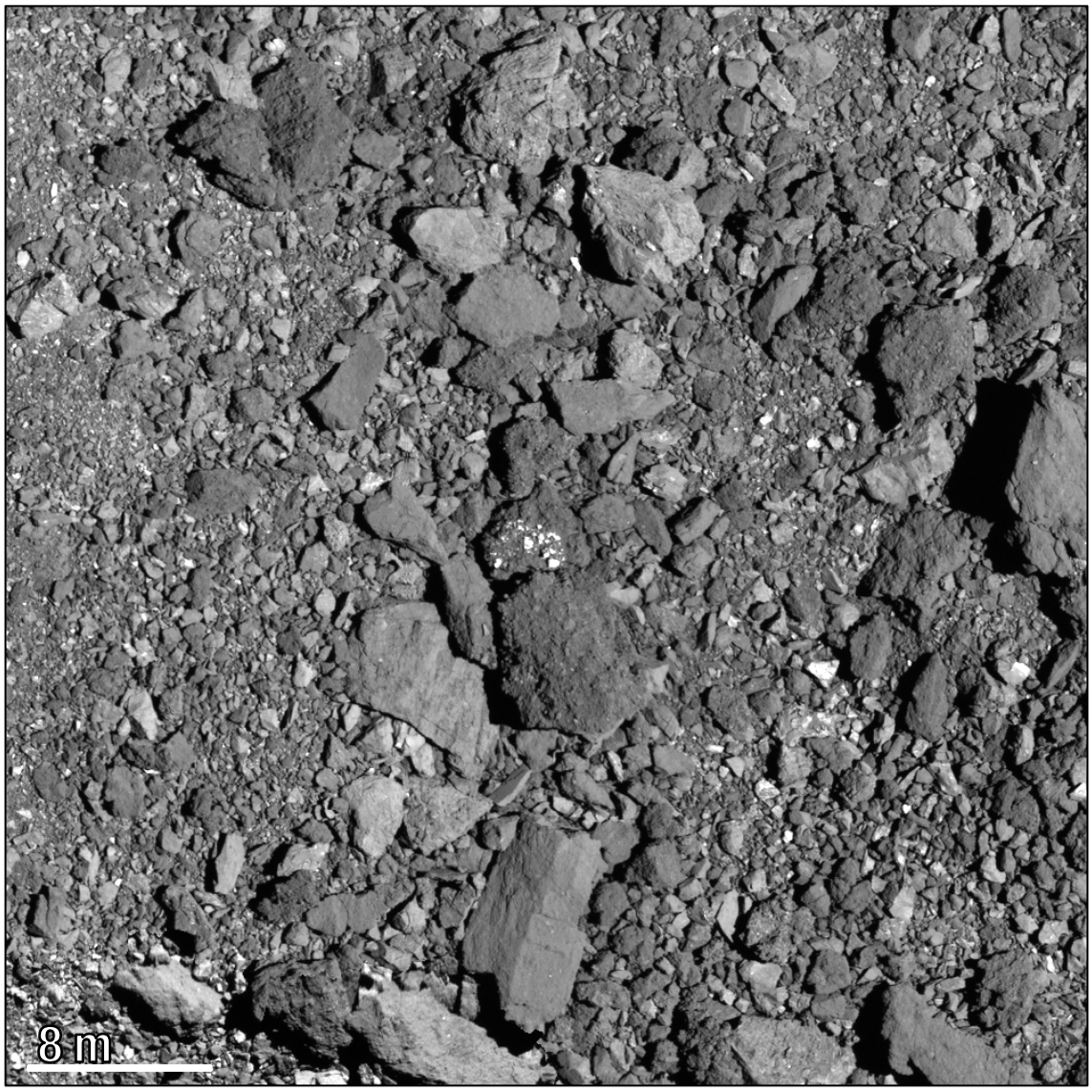

Fig S15. Regional context for the boulder shown in Fig. 3I. A 50 m × 50 m subset of the global mosaic of Bennu (*32*), centered on the boulder shown in Fig. 3I (bright clasts in a dark matrix). Although there are small bright boulders in this region, there are none in the immediate vicinity of this boulder, nor are there any on the neighboring boulders. This provides confidence that the bright clasts in the boulder shown in Fig. 3I are embedded in, rather than perched upon, the boulder.

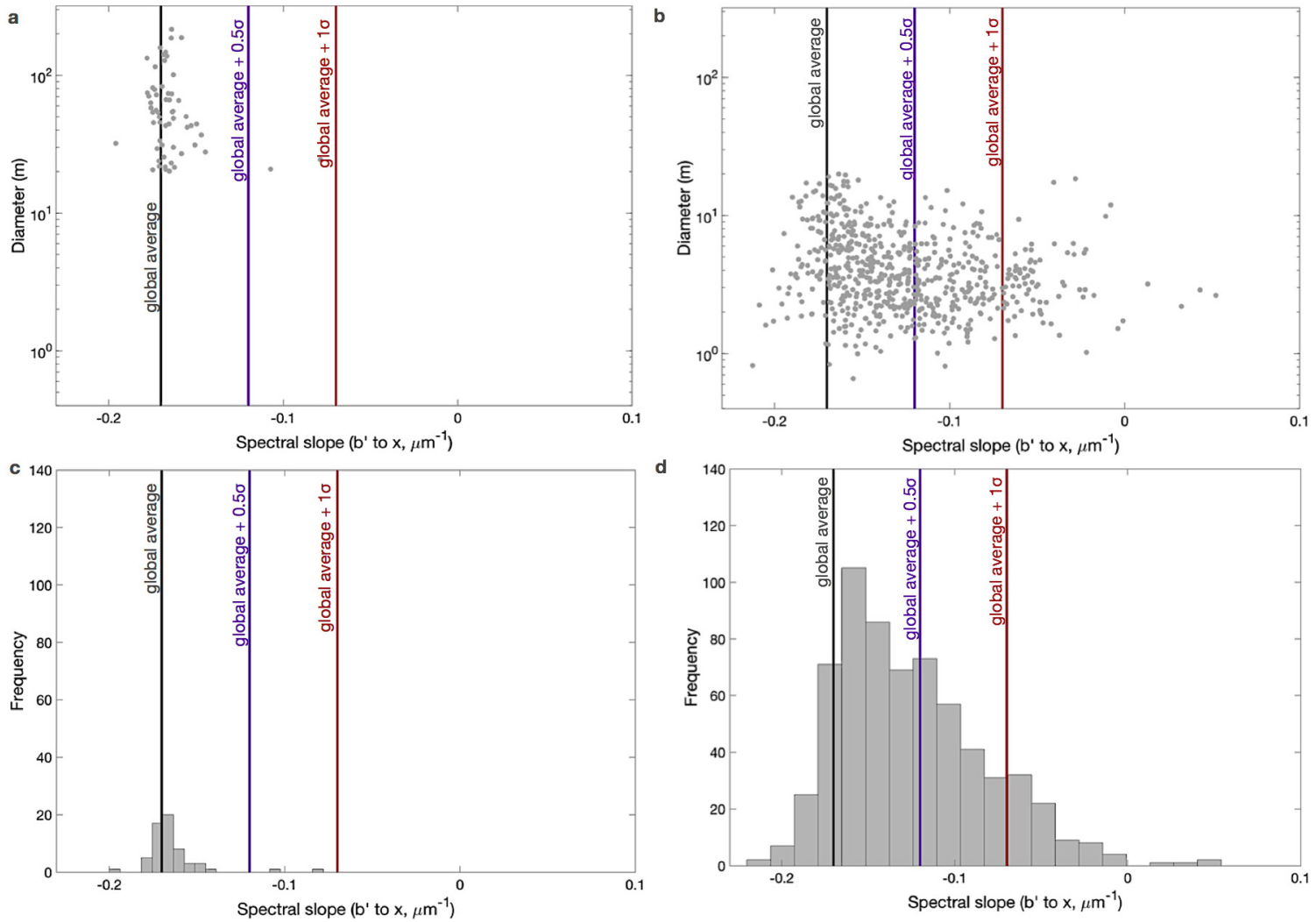

Fig S16. Supporting information for the relationship between spectral slope and crater size and frequency. (**A**) Crater diameter plotted against median b' to x spectral slope, for craters >20 m. (**B**) Crater diameter plotted against median b' to x spectral slope, for craters ≤ 20 m. (**C**) The b' to x spectral slope distribution of craters on Bennu, for craters >20 m. (**D**) The b' to x spectral slope distribution of craters on Bennu, for craters ≤20 m. When we separate out the largest craters on Bennu (>20 m), the trends between spectral slope and crater size and frequency, as highlighted in Fig. 5, still hold.

Table S1. Summary statistics obtained from the PCA performed on the four MapCam bands, including the percentage of the total variance in each PC as well as the eigenvalues, per band, for each PC.

	PC1	**PC2**	**PC3**	**PC4**
b′ eigenvalues	0.514	0.76	–0.378	0.124
v eigenvalues	0.52	0.077	0.708	–0.471
w eigenvalues	0.5	–0.373	0.18	0.76
x eigenvalues	–0.463	–0.527	–0.569	–0.429
% PC variance:	99.3	0.43	0.17	0.089

Table S2. Summary of ANOVA for different crater *b′/v* band ratios, categorized by their overall *b′* to *x* spectral slope (Fig. 6). μ is the global average *b′* to *x* spectral slope of Bennu, and σ indicates the standard deviation.

a. Summary of statistics

Category	*Count*	*Sum*	*Mean*	*Median*	*Variance*
***b′/v* band ratios for:**					
μ > craters *b′* to *x* slope	91	91.2227	1.0024	1.0028	3.57×10^{-5}
μ + 0.5σ > craters *b′-x* slope ≥ μ	366	367.3244	1.0036	1.0037	4.65×10^{-5}
μ + 1σ > craters *b′* to *x* slope ≥ μ + 0.5σ	174	175.0637	1.0061	1.0054	6.21×10^{-5}
craters *b′* to *x* slope ≥ μ + 1σ	75	75.2571	1.0034	1.0025	8.32×10^{-5}

b. ANOVA

Variation source	*Sum of squares*	*Degrees of freedom*	*Mean square*	*F*	*p-value*	F_{crit}
Between Groups	0.0011	4	0.0003	5.0612	0.0005	2.3846
Within Groups	0.0371	701	5.29×10^{-5}			
Total	0.038	705				

Caption for data S1. Comma separated value (CSV) list of the boulders used in this study. The first row are column headings and subsequent rows are boulder data. A description each column heading, in single quotes, is given parenthetically here: 'sequential_id' (arbitrary unique id), 'area_m^2' (area of the polygon used to trace boulder in units of m^2); 'center_latitude' (polygon central latitude in units of degrees, domain ±90º); 'center_longitude' (polygon central longitude in units of degrees, domain 0–360º); and 'classification' (determined by the boulder classification scheme described in this study).

Caption for data S2. CSV list of the craters used in this study. The first row are column headings and subsequent rows are crater data. A description each column heading, listed in single quotes, is given parenthetically here: 'sequential_id' (arbitrary unique id), 'radius_km' (radius of the circle used to trace the crater, in units of km); 'center_latitude' (circle central latitude in units of degrees, domain ±90º); 'center_longitude' (circle central longitude in units of degrees, domain 0–360º).

Caption for data S3. Text file list of all the OCAMS MapCam long exposure images used to produce the maps in Fig. 1.

References and Notes

1. D. S. Lauretta, S. S. Balram-Knutson, E. Beshore, W. V. Boynton, C. Drouet d'Aubigny, D. N. DellaGiustina, H. L. Enos, D. R. Golish, C. W. Hergenrother, E. S. Howell, C. A. Bennett, E. T. Morton, M. C. Nolan, B. Rizk, H. L. Roper, A. E. Bartels, B. J. Bos, J. P. Dworkin, D. E. Highsmith, D. A. Lorenz, L. F. Lim, R. Mink, M. C. Moreau, J. A. Nuth, D. C. Reuter, A. A. Simon, E. B. Bierhaus, B. H. Bryan, R. Ballouz, O. S. Barnouin, R. P. Binzel, W. F. Bottke, V. E. Hamilton, K. J. Walsh, S. R. Chesley, P. R. Christensen, B. E. Clark, H. C. Connolly, M. K. Crombie, M. G. Daly, J. P. Emery, T. J. McCoy, J. W. McMahon, D. J. Scheeres, S. Messenger, K. Nakamura-Messenger, K. Righter, S. A. Sandford, OSIRIS-REx: Sample return from asteroid (101955) Bennu. *Space Sci. Rev.* **212**, 925–984 (2017). doi:10.1007/s11214-017-0405-1

2. B. E. Clark, R. P. Binzel, E. S. Howell, E. A. Cloutis, M. Ockert-Bell, P. Christensen, M. A. Barucci, F. DeMeo, D. S. Lauretta, H. Connolly Jr., A. Soderberg, C. Hergenrother, L. Lim, J. Emery, M. Mueller, Asteroid (101955) 1999 RQ36: Spectroscopy from 0.4 to 2.4 μm and meteorite analogs. *Icarus* **216**, 462–475 (2011). doi:10.1016/j.icarus.2011.08.021

3. W. F. Bottke, D. Vokrouhlický, K. J. Walsh, M. Delbo, P. Michel, D. S. Lauretta, H. Campins, H. C. Connolly Jr., D. J. Scheeres, S. R. Chelsey, In search of the source of asteroid (101955) Bennu: Applications of the stochastic YORP model. *Icarus* **247**, 191–217 (2015). doi:10.1016/j.icarus.2014.09.046

4. D. N. DellaGiustina, J. P. Emery, D. R. Golish, B. Rozitis, C. A. Bennett, K. N. Burke, R.-L. Ballouz, K. J. Becker, P. R. Christensen, C. Y. Drouet d'Aubigny, V. E. Hamilton, D. C. Reuter, B. Rizk, A. A. Simon, E. Asphaug, J. L. Bandfield, O. S. Barnouin, M. A. Barucci, E. B. Bierhaus, R. P. Binzel, W. F. Bottke, N. E. Bowles, H. Campins, B. C. Clark, B. E. Clark, H. C. Connolly Jr., M. G. Daly, J. Leon, M. Delbo', J. D. P. Deshapriya, C. M. Elder, S. Fornasier, C. W. Hergenrother, E. S. Howell, E. R. Jawin, H. H. Kaplan, T. R. Kareta, L. Le Corre, J.-Y. Li, J. Licandro, L. F. Lim, P. Michel, J. Molaro, M. C. Nolan, M. Pajola, M. Popescu, J. L. R. Garcia, A. Ryan, S. R. Schwartz, N. Shultz, M. A. Siegler, P. H. Smith, E. Tatsumi, C. A. Thomas, K. J. Walsh, C. W. V. Wolner, X.-D. Zou, D. S. Lauretta, Properties of rubble-pile asteroid (101955) Bennu from OSIRIS-REx imaging and thermal analysis. *New Astron.* **3**, 341–351 (2019). doi:10.1038/s41550-019-0731-1

5. D. S. Lauretta, D. N. DellaGiustina, C. A. Bennett, D. R. Golish, K. J. Becker, S. S. Balram-Knutson, O. S. Barnouin, T. L. Becker, W. F. Bottke, W. V. Boynton, H. Campins, B. E. Clark, H. C. Connolly Jr., C. Y. Drouet d'Aubigny, J. P. Dworkin, J. P. Emery, H. L. Enos, V. E. Hamilton, C. W. Hergenrother, E. S. Howell, M. R. M. Izawa, H. H. Kaplan, M. C. Nolan, B. Rizk, H. L. Roper, D. J. Scheeres, P. H. Smith, K. J. Walsh, C. W. V. Wolner; OSIRIS-REx Team, The unexpected surface of asteroid (101955) Bennu. *Nature* **568**, 55–60 (2019). doi:10.1038/s41586-019-1033-6 Medline

6. O. S. Barnouin, M. G. Daly, E. E. Palmer, R. W. Gaskell, J. R. Weirich, C. L. Johnson, M. M. A. Asad, J. H. Roberts, M. E. Perry, H. C. M. Susorney, R. T. Daly, E. B. Bierhaus, J. A. Seabrook, R. C. Espiritu, A. H. Nair, L. Nguyen, G. A. Neumann, C. M. Ernst, W. V. Boynton, M. C. Nolan, C. D. Adam, M. C. Moreau, B. Risk, C. D. D'Aubigny, E. R. Jawin, K. J. Walsh, P. Michel, S. R. Schwartz, R.-L. Ballouz, E. M. Mazarico, D. J.

Scheeres, J. McMahon, W. Bottke, S. Sugita, N. Hirata, N. Hirata, S. Watanabe, K. N. Burke, D. N. DellaGuistina, C. A. Bennett, D. S. Lauretta; OSIRIS-REx Team., Shape of (101955) Bennu indicative of a rubble pile with internal stiffness. *Nat. Geosci.* **12**, 247–252 (2019). doi:10.1038/s41561-019-0330-x Medline

7. V. E. Hamilton, A. A. Simon, P. R. Christensen, D. C. Reuter, B. E. Clark, M. A. Barucci, N. E. Bowles, W. V. Boynton, J. R. Brucato, E. A. Cloutis, H. C. Connolly Jr., K. L. D. Hanna, J. P. Emery, H. L. Enos, S. Fornasier, C. W. Haberle, R. D. Hanna, E. S. Howell, H. H. Kaplan, L. P. Keller, C. Lantz, J.-Y. Li, L. F. Lim, T. J. McCoy, F. Merlin, M. C. Nolan, A. Praet, B. Rozitis, S. A. Sandford, D. L. Schrader, C. A. Thomas, X.-D. Zou, D. S. Lauretta; OSIRIS-REx Team, Evidence for widespread hydrated minerals on asteroid (101955) Bennu. *Nat. Astron.* **3**, 332–340 (2019). doi:10.1038/s41550-019-0722-2 Medline

8. A. A. Simon, H. H. Kaplan, V. E. Hamilton, D. S. Lauretta, H. Campins, J. P. Emery, M. A. Barucci, D. N. DellaGiustina, D. C. Reuter, S. A. Sandford, D. R. Golish, L. F. Lim, A. Ryan, B. Rozitis, C. A. Bennett, Widespread carbon-bearing materials on near-Earth asteroid (101955) Bennu. *Science* 10.1126/science.abc3522 (2020). doi:10.1126/science.abc3522

9. H. H. Kaplan, D. S. Lauretta, A. A. Simon, V. E. Hamilton, D. N. DellaGiustina, D. R. Golish, D. C. Reuter, C. A. Bennett, K. N. Burke, H. Campins, H. C. Connolly Jr., J. P. Dworkin, J. P. Emery, D. P. Glavin, T. D. Glotch, R. Hanna, K. Ishimaru, E. R. Jawin, T. J. McCoy, N. Porter, S. A. Sandford, S. Ferrone, B. E. Clark, J.-Y. Li, X.-D. Zou, M. G. Daly, O. S. Barnouin, J. A. Seabrook, H. L. Enos, Bright carbonate veins on asteroid (101955) Bennu: Implications for aqueous alteration history. *Science* 10.1126/science.abc3557 (2020). doi:10.1126/science.abc3557

10. C. W. Hergenrother, C. K. Maleszewski, M. C. Nolan, J.-Y. Li, C. Y. Drouet d'Aubigny, F. C. Shelly, E. S. Howell, T. R. Kareta, M. R. M. Izawa, M. A. Barucci, E. B. Bierhaus, H. Campins, S. R. Chesley, B. E. Clark, E. J. Christensen, D. N. DellaGiustina, S. Fornasier, D. R. Golish, C. M. Hartzell, B. Rizk, D. J. Scheeres, P. H. Smith, X.-D. Zou, D. S. Lauretta; OSIRIS-REx Team, The operational environment and rotational acceleration of asteroid (101955) Bennu from OSIRIS-REx observations. *Nat. Commun.* **10**, 1291 (2019). doi:10.1038/s41467-019-09213-x Medline

11. A. E. Saal, E. H. Hauri, J. A. Van Orman, M. J. Rutherford, Hydrogen isotopes in lunar volcanic glasses and melt inclusions reveal a carbonaceous chondrite heritage. *Science* **340**, 1317–1320 (2013). doi:10.1126/science.1235142 Medline

12. C. R. Chapman, J. W. Salisbury, Comparisons of meteorite and asteroid spectral reflectivities. *Icarus* **19**, 507–522 (1973). doi:10.1016/0019-1035(73)90078-X

13. D. Nesvorný, R. Jedicke, R. J. Whiteley, Ž. Ivezić, Evidence for asteroid space weathering from the Sloan Digital Sky Survey. *Icarus* **173**, 132–152 (2005). doi:10.1016/j.icarus.2004.07.026

14. M. J. Gaffey, J. F. Bell, R. H. Brown, T. H. Burbine, J. L. Piatek, K. L. Reed, D. A. Chaky, Mineralogical variations within the S-type asteroid class. *Icarus* **106**, 573–602 (1993). doi:10.1006/icar.1993.1194

15. M. Lazzarin, S. Marchi, L. V. Moroz, R. Brunetto, S. Magrin, P. Paolicchi, G. Strazzulla, Space weathering in the main asteroid belt: The big picture. *Astrophys. J.* **647**, L179–L182 (2006). doi:10.1086/507448

16. H. M. Kaluna, J. R. Masiero, K. J. Meech, Space weathering trends among carbonaceous asteroids. *Icarus* **264**, 62–71 (2016). doi:10.1016/j.icarus.2015.09.007

17. R. Brunetto, M. J. Loeffler, D. Nesvorný, S. Sasaki, G. Strazzulla, "Asteroid surface alteration by space weathering processes" in *Asteroids IV*, 597–616 (2015).http://dx.doi.org/10.2458/azu_uapress_9780816532131-ch031

18. P. Vernazza, D. Fulvio, R. Brunetto, J. P. Emery, C. A. Dukes, F. Cipriani, O. Witasse, M. J. Schaible, B. Zanda, G. Strazzulla, R. A. Baragiola, Paucity of Tagish Lake-like parent bodies in the Asteroid Belt and among Jupiter Trojans. *Icarus* **225**, 517–525 (2013). doi:10.1016/j.icarus.2013.04.019

19. M. Matsuoka, T. Nakamura, Y. Kimura, T. Hiroi, R. Nakamura, S. Okumura, S. Sasaki, Pulse-laser irradiation experiments of Murchison CM2 chondrite for reproducing space weathering on C-type asteroids. *Icarus* **254**, 135–143 (2015). doi:10.1016/j.icarus.2015.02.029

20. C. Lantz, R. Brunetto, M. A. Barucci, S. Fornasier, D. Baklouti, J. Bourçois, M. Godard, Ion irradiation of carbonaceous chondrites: A new view of space weathering on primitive asteroids. *Icarus* **285**, 43–57 (2017). doi:10.1016/j.icarus.2016.12.019

21. C. Lantz, R. P. Binzel, F. E. DeMeo, Space weathering trends on carbonaceous asteroids: A possible explanation for Bennu's blue slope? *Icarus* **302**, 10–17 (2018). doi:10.1016/j.icarus.2017.11.010

22. M. S. Thompson, R. V. Morris, S. J. Clemett, M. J. Loeffler, D. Trang, L. P. Keller, R. Christoffersen, D. G. Agresti, The effect of progressive space weathering on the organic and inorganic components of a carbonaceous chondrite. *Icarus* **346**, 113775 (2020). doi:10.1016/j.icarus.2020.113775

23. H. M. Kaluna, H. A. Ishii, J. P. Bradley, J. J. Gillis-Davis, P. G. Lucey, Simulated space weathering of Fe-and Mg-rich aqueously altered minerals using pulsed laser irradiation. *Icarus* **292**, 245–258 (2017). doi:10.1016/j.icarus.2016.12.028

24. M. S. Thompson, M. J. Loeffler, R. V. Morris, L. P. Keller, R. Christoffersen, Spectral and chemical effects of simulated space weathering of the Murchison CM2 carbonaceous chondrite. *Icarus* **319**, 499–511 (2019). doi:10.1016/j.icarus.2018.09.022

25. D. N. DellaGiustina, C. A. Bennett, K. Becker, D. R. Golish, L. Le Corre, D. A. Cook, K. L. Edmundson, M. Chojnacki, S. S. Sutton, M. P. Milazzo, B. Carcich, M. C. Nolan, N. Habib, K. N. Burke, T. Becker, P. H. Smith, K. J. Walsh, K. Getzandanner, D. R. Wibben, J. M. Leonard, M. M. Westermann, A. T. Polit, J. N. Kidd Jr., C. W. Hergenrother, W. V. Boynton, J. Backer, S. Sides, J. Mapel, K. Berry, H. Roper, C. Drouet d'Aubigny, B. Rizk, M. K. Crombie, E. K. Kinney-Spano, J. de León, J. L. Rizos, J. Licandro, H. C. Campins, B. E. Clark, H. L. Enos, D. S. Lauretta, Overcoming the challenges associated with image-based mapping of small bodies in preparation for the OSIRIS-REx mission to (101955) Bennu. *Earth Space Sci.* **5**, 929–949 (2018). doi:10.1029/2018EA000382

26. B. Rizk, C. Drouet d'Aubigny, D. Golish, C. Fellows, C. Merrill, P. Smith, M. S. Walker, J. E. Hendershot, J. Hancock, S. H. Bailey, D. N. DellaGiustina, D. S. Lauretta, R. Tanner, M. Williams, K. Harshman, M. Fitzgibbon, W. Verts, J. Chen, T. Connors, D. Hamara, A. Dowd, A. Lowman, M. Dubin, R. Burt, M. Whiteley, M. Watson, T. McMahon, M. Ward, D. Booher, M. Read, B. Williams, M. Hunten, E. Little, T. Saltzman, D. Alfred, S. O'Dougherty, M. Walthall, K. Kenagy, S. Peterson, B. Crowther, M. L. Perry, C. See, S. Selznick, C. Sauve, M. Beiser, W. Black, R. N. Pfisterer, A. Lancaster, S. Oliver, C. Oquest, D. Crowley, C. Morgan, C. Castle, R. Dominguez, M. Sullivan, OCAMS: The OSIRIS-REx camera suite. *Space Sci. Rev.* **214**, 26 (2018). doi:10.1007/s11214-017-0460-7

27. B. Zellner, D. J. Tholen, E. F. Tedesco, The eight-color asteroid survey: Results for 589 minor planets. *Icarus* **61**, 355–416 (1985). doi:10.1016/0019-1035(85)90133-2

28. F. E. DeMeo, B. Carry, The taxonomic distribution of asteroids from multi-filter all-sky photometric surveys. *Icarus* **226**, 723–741 (2013). doi:10.1016/j.icarus.2013.06.027

29. D. R. Golish, C. Drouet d'Aubigny, B. Rizk, D. N. DellaGiustina, P. H. Smith, K. Becker, N. Shultz, T. Stone, M. K. Barker, E. Mazarico, E. Tatsumi, R. W. Gaskell, L. Harrison, C. Merrill, C. Fellows, B. Williams, S. O'Dougherty, M. Whiteley, J. Hancock, B. E. Clark, C. W. Hergenrother, D. S. Lauretta, Ground and In-Flight Calibration of the OSIRIS-REx Camera Suite. *Space Sci. Rev.* **216**, 12 (2020). doi:10.1007/s11214-019-0626-6 Medline

30. D. R. Golish, D. N. DellaGiustina, J.-Y. Li, B. E. Clark, X.-D. Zou, P. H. Smith, J. L. Rizos, P. H. Hasselmann, C. A. Bennett, S. Fornasier, R.-L. Ballouz, C. Drouet d'Aubigny, B. Rizk, M. G. Daly, O. S. Barnouin, L. Philpott, M. M. Al Asad, J. A. Seabrook, C. L. Johnson, D. S. Lauretta, Disk-resolved photometric modeling and properties of asteroid (101955) Bennu. *Icarus* 10.1016/j.icarus.2020.113724 (2020). doi:10.1016/j.icarus.2020.113724

31. Materials and methods are available as supplementary materials.

32. C. A. Bennett, D. N. DellaGiustina, K. J. Becker, T. L. Becker, K. L. Edmundson, D. R. Golish, R. J. Bennett, K. N. Burke, C. N. U. Cue, B. E. Clark, J. Contreras, J. D. P. Deshapriya, C. D. d'Aubigny, G. Fitzgibbon, E. R. Jawin, T. Q. Nolan, N. A. Porter, M. M. Riehl, H. L. Roper, B. Rizk, Y. Tang, Z. Zeszut, R. W. Gaskell, E. E. Palmer, J. R. Weirich, M. M. Al Asad, L. Philpott, M. G. Daly, O. S. Barnouin, H. L. Enos, D. S. Lauretta, A high-resolution global basemap of (101955) Bennu. *Icarus* 10.1016/j.icarus.2020.113690 (2020). doi:10.1016/j.icarus.2020.113690

33. K. J. Walsh, E. R. Jawin, R.-L. Ballouz, O. S. Barnouin, E. B. Bierhaus, H. C. Connolly Jr., J. L. Molaro, T. J. McCoy, M. Delbo', C. M. Hartzell, M. Pajola, S. R. Schwartz, D. Trang, E. Asphaug, K. J. Becker, C. B. Beddingfield, C. A. Bennett, W. F. Bottke, K. N. Burke, B. C. Clark, M. G. Daly, D. N. DellaGiustina, J. P. Dworkin, C. M. Elder, D. R. Golish, A. R. Hildebrand, R. Malhotra, J. Marshall, P. Michel, M. C. Nolan, M. E. Perry, B. Rizk, A. Ryan, S. A. Sandford, D. J. Scheeres, H. C. M. Susorney, F. Thuillet, D. S. Lauretta, Craters, boulders and regolith of (101955) Bennu indicative of an old and dynamic surface. *Nat. Geosci.* **12**, 242–246 (2019). doi:10.1038/s41561-019-0326-6

34. M. G. Daly, O. S. Barnouin, C. Dickinson, J. Seabrook, C. L. Johnson, G. Cunningham, T. Haltigin, D. Gaudreau, C. Brunet, I. Aslam, A. Taylor, E. B. Bierhaus, W. Boynton, M.

Nolan, D. S. Lauretta, The OSIRIS-REx laser altimeter (OLA) investigation and instrument. *Space Sci. Rev.* **212**, 899–924 (2017). doi:10.1007/s11214-017-0375-3

35. O. S. Barnouin, M. G. Daly, E. E. Palmer, C. L. Johnson, R. W. Gaskell, M. Al Asad, E. B. Bierhaus, K. L. Craft, C. M. Ernst, R. C. Espiritu, H. Nair, G. A. Neumann, L. Nguyen, M. C. Nolan, E. Mazarico, M. E. Perry, L. C. Philpott, J. H. Roberts, R. J. Steele, J. Seabrook, H. C. M. Susorney, J. R. Weirich, D. S. Lauretta, Digital terrain mapping by the OSIRIS-REx mission. *Planet. Space Sci.* **180**, 104764 (2020). doi:10.1016/j.pss.2019.104764

36. M. G. Daly, O. S. Barnouin, J. A. Seabrook, J. Roberts, C. Dickinson, K. J. Walsh, E. R. Jawin, E. E. Palmer, R. Gaskell, J. Weirich, T. Haltigin, D. Gaudreau, C. Brunet, G. Cunningham, P. Michel, Y. Zhang, R.-L. Ballouz, G. Neumann, M. E. Perry, L. Philpott, M. M. Al Asad, C. L. Johnson, C. D. Adam, J. M. Leonard, J. L. Geeraert, K. Getzandanner, M. C. Nolan, R. T. Daly, E. B. Bierhaus, E. Mazarico, B. Rozitis, A. J. Ryan, D. N. Dellaguistina, B. Rizk, H. C. M. Susorney, H. L. Enos, D. S. Lauretta, Hemispherical differences in the shape and topography of asteroid (101955) Bennu. *Sci. Adv.* **6**, eabd3649 (2020). doi:10.1126/sciadv.abd3649

37. D. C. Reuter, A. A. Simon, J. Hair, A. Lunsford, S. Manthripragada, V. Bly, B. Bos, C. Brambora, E. Caldwell, G. Casto, Z. Dolch, P. Finneran, D. Jennings, M. Jhabvala, E. Matson, M. McLelland, W. Roher, T. Sullivan, E. Weigle, Y. Wen, D. Wilson, D. S. Lauretta, The OSIRIS-REx Visible and InfraRed Spectrometer (OVIRS): Spectral maps of the asteroid Bennu. *Space Sci. Rev.* **214**, 54 (2018). doi:10.1007/s11214-018-0482-9

38. D. N. DellaGiustina, H. H. Kaplan, A. A. Simon, W. F. Bottke, C. Avdellidou, M. Delbo, R.-L. Ballouz, D. R. Golish, K. J. Walsh, M. Popescu, H. Campins, M. A. Barucci, G. Poggiali, R. T. Daly, L. Le Corre, V. E. Hamilton, N. Porter, E. R. Jawin, T. J. McCoy, H. C. Connolly Jr., J. L. R. Garcia, E. Tatsumi, J. de Leon, J. Licandro, S. Fornasier, M. G. Daly, M. M. Al Asad, L. Philpott, J. Seabrook, O. S. Barnouin, B. E. Clark, M. C. Nolan, E. S. Howell, R. P. Binzel, B. Rizk, D. C. Reuter, D. S. Lauretta, Exogenic Basalt on Asteroid (101955) Bennu. *New Astron.* (2020). doi:10.1038/s41550-020-1195-z

39. J. L. Molaro, K. J. Walsh, E. R. Jawin, R.-L. Ballouz, C. A. Bennett, D. N. DellaGiustina, D. R. Golish, C. Drouet d'Aubigny, B. Rizk, S. R. Schwartz, R. D. Hanna, S. J. Martel, M. Pajola, H. Campins, A. J. Ryan, W. F. Bottke, D. S. Lauretta, In situ evidence of thermally induced rock breakdown widespread on Bennu's surface. *Nat. Commun.* **11**, 2913 (2020). doi:10.1038/s41467-020-16528-7 Medline

40. C. T. Russell, C. A. Raymond, A. Coradini, H. Y. McSween, M. T. Zuber, A. Nathues, M. C. De Sanctis, R. Jaumann, A. S. Konopliv, F. Preusker, S. W. Asmar, R. S. Park, R. Gaskell, H. U. Keller, S. Mottola, T. Roatsch, J. E. C. Scully, D. E. Smith, P. Tricarico, M. J. Toplis, U. R. Christensen, W. C. Feldman, D. J. Lawrence, T. J. McCoy, T. H. Prettyman, R. C. Reedy, M. E. Sykes, T. N. Titus, Dawn at Vesta: Testing the protoplanetary paradigm. *Science* **336**, 684–686 (2012). doi:10.1126/science.1219381 Medline

41. F. Vilas, A cheaper, faster, better way to detect water of hydration on Solar System bodies. *Icarus* **111**, 456–467 (1994). doi:10.1006/icar.1994.1156

42. D. S. Lauretta, C. W. Hergenrother, S. R. Chesley, J. M. Leonard, J. Y. Pelgrift, C. D. Adam, M. Al Asad, P. G. Antreasian, R.-L. Ballouz, K. J. Becker, C. A. Bennett, B. J. Bos, W. F. Bottke, M. Brozović, H. Campins, H. C. Connolly Jr., M. G. Daly, A. B. Davis, J. de León, D. N. DellaGiustina, C. Y. Drouet d'Aubigny, J. P. Dworkin, J. P. Emery, D. Farnocchia, D. P. Glavin, D. R. Golish, C. M. Hartzell, R. A. Jacobson, E. R. Jawin, P. Jenniskens, J. N. Kidd Jr., E. J. Lessac-Chenen, J.-Y. Li, G. Libourel, J. Licandro, A. J. Liounis, C. K. Maleszewski, C. Manzoni, B. May, L. K. McCarthy, J. W. McMahon, P. Michel, J. L. Molaro, M. C. Moreau, D. S. Nelson, W. M. Owen Jr., B. Rizk, H. L. Roper, B. Rozitis, E. M. Sahr, D. J. Scheeres, J. A. Seabrook, S. H. Selznick, Y. Takahashi, F. Thuillet, P. Tricarico, D. Vokrouhlický, C. W. V. Wolner, Episodes of particle ejection from the surface of the active asteroid (101955) Bennu. *Science* **366**, eaay3544 (2019). doi:10.1126/science.aay3544 Medline

43. E. R. Jawin, K. J. Walsh, O. S. Barnouin, T. J. McCoy, R.-L. Ballouz, D. N. DellaGiustina, H. C. Connolly Jr., J. Marshall, C. Beddingfield, M. C. Nolan, J. L. Molaro, C. A. Bennett, D. J. Scheeres, M. G. Daly, M. Al Asad, R. T. Daly, E. B. Bierhaus, H. C. M. Susorney, H. H. Kaplan, H. L. Enos, D. S. Lauretta, Global patterns of mass movement on asteroid (101955) Bennu. *J. Geophys. Res. Planets* **125**, e2020JE006475 (2020). doi:10.1029/2020JE006475

44. A. R. Hendrix, F. Vilas, C-complex asteroids: UV-visible spectral characteristics and implications for space weathering effects. *Geophys. Res. Lett.* **46**, 14307–14317 (2019). doi:10.1029/2019GL085883

45. W. F. Bottke Jr., D. Durda, D. Nesvorny, R. Jedicke, A. Morbidelli, D. Vokrouhlicky, H. Levison, Linking the collisional history of the main asteroid belt to its dynamical excitation and depletion. *Icarus* **179**, 63–94 (2005). doi:10.1016/j.icarus.2005.05.017

46. S. Marchi, C. Barbieri, M. Küppers, F. Marzari, B. Davidsson, H. U. Keller, S. Besse, P. Lamy, S. Mottola, M. Massironi, G. Cremonese, The cratering history of asteroid (2867) Steins. *Planet. Space Sci.* **58**, 1116–1123 (2010). doi:10.1016/j.pss.2010.03.017

47. P. Brown, R. E. Spalding, D. O. ReVelle, E. Tagliaferri, S. P. Worden, The flux of small near-Earth objects colliding with the Earth. *Nature* **420**, 294–296 (2002). doi:10.1038/nature01238 Medline

48. A. W. Harris, G. D'Abramo, The population of near-Earth asteroids. *Icarus* **257**, 302–312 (2015). doi:10.1016/j.icarus.2015.05.004

49. S. Marchi, C. R. Chapman, O. S. Barnouin, J. E. Richardson, J. Vincent, "Cratering on asteroids" *Asteroids IV*, 725–744 (2015).

50. M. Arakawa, T. Saiki, K. Wada, K. Ogawa, T. Kadono, K. Shirai, H. Sawada, K. Ishibashi, R. Honda, N. Sakatani, Y. Iijima, C. Okamoto, H. Yano, Y. Takagi, M. Hayakawa, P. Michel, M. Jutzi, Y. Shimaki, S. Kimura, Y. Mimasu, T. Toda, H. Imamura, S. Nakazawa, H. Hayakawa, S. Sugita, T. Morota, S. Kameda, E. Tatsumi, Y. Cho, K. Yoshioka, Y. Yokota, M. Matsuoka, M. Yamada, T. Kouyama, C. Honda, Y. Tsuda, S. Watanabe, M. Yoshikawa, S. Tanaka, F. Terui, S. Kikuchi, T. Yamaguchi, N. Ogawa, G. Ono, K. Yoshikawa, T. Takahashi, Y. Takei, A. Fujii, H. Takeuchi, Y. Yamamoto, T. Okada, C. Hirose, S. Hosoda, O. Mori, T. Shimada, S. Soldini, R. Tsukizaki, T. Iwata, M. Ozaki, M. Abe, N. Namiki, K. Kitazato, S. Tachibana, H. Ikeda, N. Hirata, N. Hirata, R.

Noguchi, A. Miura, An artificial impact on the asteroid (162173) Ryugu formed a crater in the gravity-dominated regime. *Science* **368**, 67–71 (2020). doi:10.1126/science.aaz1701 Medline

51. E. Tatsumi, S. Sugita, Cratering efficiency on coarse-grain targets: Implications for the dynamical evolution of asteroid 25143 Itokawa. *Icarus* **300**, 227–248 (2018). doi:10.1016/j.icarus.2017.09.004

52. L. P. Keller, E. L. Berger, A transmission electron microscope study of Itokawa regolith grains. *Earth Planets Space* **66**, 71 (2014). doi:10.1186/1880-5981-66-71

53. T. V. Johnson, F. P. Fanale, Optical properties of carbonaceous chondrites and their relationship to asteroids. *J. Geophys. Res.* **78**, 8507–8518 (1973). doi:10.1029/JB078i035p08507

54. C. M. Hartzell, Dynamics of 2D electrostatic dust levitation at asteroids. *Icarus* **333**, 234–242 (2019). doi:10.1016/j.icarus.2019.05.013

55. M. C. Nolan, E. S. Howell, D. J. Scheeres, J. W. McMahon, O. Golubov, C. W. Hergenrother, J. P. Emery, K. S. Noll, S. R. Chesley, D. S. Lauretta, Detection of rotational acceleration of Bennu using HST light curve observations. *Geophys. Res. Lett.* **46**, 1956–1962 (2019). doi:10.1029/2018GL080658

56. W. F. Bottke, A. V. Moorhead, H. C. Connolly Jr., C. W. Hergenrother, J. L. Molaro, P. Michel, M. C. Nolan, S. R. Schwartz, D. Vokrouhlický, K. J. Walsh, D. S. Lauretta, Meteoroid Impacts as a Source of Bennu's Particle Ejection Events. *J. Geophys. Res. Planets* **125**, e2019JE006282 (2020). doi:10.1029/2019JE006282

57. L. Moroz, G. Baratta, G. Strazzulla, L. Starukhina, E. Dotto, M. A. Barucci, G. Arnold, E. Distefano, Optical alteration of complex organics induced by ion irradiation: 1. Laboratory experiments suggest unusual space weathering trend. *Icarus* **170**, 214–228 (2004). doi:10.1016/j.icarus.2004.02.003

58. B. Hapke, Space weathering from Mercury to the asteroid belt. *J. Geophys. Res. Planets* **106**, 10039–10073 (2001). doi:10.1029/2000JE001338

59. A. S. Rivkin, E. S. Howell, F. Vilas, L. A. Lebofsky, "Hydrated Minerals on Asteroids: The Astronomical Record" *Asteroids III* **1**, 235–253 (2002).

60. B. Rozitis, A. J. Ryan, J. P. Emery, P. R. Christensen, V. E. Hamilton, A. A. Simon, D. C. Reuter, M. Al Asad, R.-L. Ballouz, J. L. Bandfield, O. S. Barnouin, C. A. Bennett, M. Bernacki, K. N. Burke, S. Cambioni, B. E. Clark, M. G. Daly, M. Delbo, D. N. DellaGiustina, C. M. Elder, R. D. Hanna, C. W. Haberle, E. S. Howell, D. R. Golish, E. R. Jawin, H. H. Kaplan, L. F. Lim, J. L. Molaro, D. P. Munoz, M. C. Nolan, B. Rizk, M. A. Siegler, H. C. M. Susorney, K. J. Walsh, D. S. Lauretta, Asteroid (101955) Bennu's weak boulders and thermally anomalous equator. *Sci. Adv.* **6**, eabc3699 (2020). doi:10.1126/sciadv.abc3699

61. C. A. Johnson, M. Prinz, Carbonate compositions in CM and CI chondrites and implications for aqueous alteration. *Geochim. Cosmochim. Acta* **57**, 2843–2852 (1993). doi:10.1016/0016-7037(93)90393-B

62. A. Morlok, A. Bischoff, T. Stephan, C. Floss, E. Zinner, E. K. Jessberger, Brecciation and chemical heterogeneities of CI chondrites. *Geochim. Cosmochim. Acta* **70**, 5371–5394 (2006). doi:10.1016/j.gca.2006.08.007

63. J. Alfing, M. Patzek, A. Bischoff, Modal abundances of coarse-grained (> 5 μm) components within CI-chondrites and their individual clasts–Mixing of various lithologies on the CI parent body(ies). *Geochemistry* **79**, 125532 (2019). doi:10.1016/j.chemer.2019.08.004

64. E. A. Cloutis, M. R. M. Izawa, L. Pompilio, V. Reddy, H. Hiesinger, A. Nathues, P. Mann, L. Le Corre, E. Palomba, J. F. Bell III, Spectral reflectance properties of HED meteorites CM2 carbonaceous chondrites: Comparison to HED grain size and compositional variations and implications for the nature of low-albedo features on Asteroid 4 Vesta. *Icarus* **223**, 850–877 (2013). doi:10.1016/j.icarus.2013.02.003

65. M. R. Izawa, E. A. Cloutis, T. Rhind, S. A. Mertzman, D. M. Applin, J. M. Stromberg, D. M. Sherman, Spectral reflectance properties of magnetites: Implications for remote sensing. *Icarus* **319**, 525–539 (2019). doi:10.1016/j.icarus.2018.10.002

66. C. M. Alexander, R. Bowden, M. L. Fogel, K. T. Howard, Carbonate abundances and isotopic compositions in chondrites. *Meteorit. Planet. Sci.* **50**, 810–833 (2015). doi:10.1111/maps.12410

67. J. de León, H. Campins, D. Morate, M. De Prá, V. Alí-Lagoa, J. Licandro, J. L. Rizos, N. Pinilla-Alonso, D. N. DellaGiustina, D. S. Lauretta, M. Popescu, V. Lorenzi, Expected spectral characteristics of (101955) Bennu and (162173) Ryugu, targets of the OSIRIS-REx and Hayabusa2 missions. *Icarus* **313**, 25–37 (2018). doi:10.1016/j.icarus.2018.05.009

68. S. Sugita, R. Honda, T. Morota, S. Kameda, H. Sawada, E. Tatsumi, M. Yamada, C. Honda, Y. Yokota, T. Kouyama, N. Sakatani, K. Ogawa, H. Suzuki, T. Okada, N. Namiki, S. Tanaka, Y. Iijima, K. Yoshioka, M. Hayakawa, Y. Cho, M. Matsuoka, N. Hirata, N. Hirata, H. Miyamoto, D. Domingue, M. Hirabayashi, T. Nakamura, T. Hiroi, T. Michikami, P. Michel, R.-L. Ballouz, O. S. Barnouin, C. M. Ernst, S. E. Schröder, H. Kikuchi, R. Hemmi, G. Komatsu, T. Fukuhara, M. Taguchi, T. Arai, H. Senshu, H. Demura, Y. Ogawa, Y. Shimaki, T. Sekiguchi, T. G. Müller, A. Hagermann, T. Mizuno, H. Noda, K. Matsumoto, R. Yamada, Y. Ishihara, H. Ikeda, H. Araki, K. Yamamoto, S. Abe, F. Yoshida, A. Higuchi, S. Sasaki, S. Oshigami, S. Tsuruta, K. Asari, S. Tazawa, M. Shizugami, J. Kimura, T. Otsubo, H. Yabuta, S. Hasegawa, M. Ishiguro, S. Tachibana, E. Palmer, R. Gaskell, L. Le Corre, R. Jaumann, K. Otto, N. Schmitz, P. A. Abell, M. A. Barucci, M. E. Zolensky, F. Vilas, F. Thuillet, C. Sugimoto, N. Takaki, Y. Suzuki, H. Kamiyoshihara, M. Okada, K. Nagata, M. Fujimoto, M. Yoshikawa, Y. Yamamoto, K. Shirai, R. Noguchi, N. Ogawa, F. Terui, S. Kikuchi, T. Yamaguchi, Y. Oki, Y. Takao, H. Takeuchi, G. Ono, Y. Mimasu, K. Yoshikawa, T. Takahashi, Y. Takei, A. Fujii, C. Hirose, S. Nakazawa, S. Hosoda, O. Mori, T. Shimada, S. Soldini, T. Iwata, M. Abe, H. Yano, R. Tsukizaki, M. Ozaki, K. Nishiyama, T. Saiki, S. Watanabe, Y. Tsuda, The geomorphology, color, and thermal properties of Ryugu: Implications for parent-body processes. *Science* **364**, 252 (2019). doi:10.1126/science.aaw0422 Medline

69. C. W. Hergenrother, C. Maleszewski, J.-Y. Li, M. Pajola, S. R. Chesley, A. S. French, A. B. Davis, J. Y. Pelgrift, J. M. Leonard, F. Shelly, A. J. Liounis, K. Becker, S. S. Balram-

Knutson, R. Garcia, T. R. Kareta, C. Adam, K. Alkiek, B. J. Bos, M. Brozović, K. N. Burke, E. Christensen, B. E. Clark, D. N. DellaGiustina, C. Drouet d'Aubigny, D. Farnocchia, E. S. Howell, R. A. Jacobson, J. N. Kidd, E. J. Lessac-Chenen, R. Melikyan, M. C. Nolan, R. S. Park, S. Selznick, B. Rizk, D. S. Lauretta, Photometry of particles ejected from active asteroid (101955) Bennu. *J. Geophys. Res. Planets* **125**, e2020JE006381 (2020). doi:10.1029/2020JE006381

70. T. Morota, S. Sugita, Y. Cho, M. Kanamaru, E. Tatsumi, N. Sakatani, R. Honda, N. Hirata, H. Kikuchi, M. Yamada, Y. Yokota, S. Kameda, M. Matsuoka, H. Sawada, C. Honda, T. Kouyama, K. Ogawa, H. Suzuki, K. Yoshioka, M. Hayakawa, N. Hirata, M. Hirabayashi, H. Miyamoto, T. Michikami, T. Hiroi, R. Hemmi, O. S. Barnouin, C. M. Ernst, K. Kitazato, T. Nakamura, L. Riu, H. Senshu, H. Kobayashi, S. Sasaki, G. Komatsu, N. Tanabe, Y. Fujii, T. Irie, M. Suemitsu, N. Takaki, C. Sugimoto, K. Yumoto, M. Ishida, H. Kato, K. Moroi, D. Domingue, P. Michel, C. Pilorget, T. Iwata, M. Abe, M. Ohtake, Y. Nakauchi, K. Tsumura, H. Yabuta, Y. Ishihara, R. Noguchi, K. Matsumoto, A. Miura, N. Namiki, S. Tachibana, M. Arakawa, H. Ikeda, K. Wada, T. Mizuno, C. Hirose, S. Hosoda, O. Mori, T. Shimada, S. Soldini, R. Tsukizaki, H. Yano, M. Ozaki, H. Takeuchi, Y. Yamamoto, T. Okada, Y. Shimaki, K. Shirai, Y. Iijima, H. Noda, S. Kikuchi, T. Yamaguchi, N. Ogawa, G. Ono, Y. Mimasu, K. Yoshikawa, T. Takahashi, Y. Takei, A. Fujii, S. Nakazawa, F. Terui, S. Tanaka, M. Yoshikawa, T. Saiki, S. Watanabe, Y. Tsuda, Sample collection from asteroid (162173) Ryugu by Hayabusa2: Implications for surface evolution. *Science* **368**, 654–659 (2020). doi:10.1126/science.aaz6306 Medline

71. K. Kitazato *et al*., Asteroid 162173 Ryugu: Surface composition as observed by Hayabusa2/NIRS3, 13, EPSC-DPS2019-1376-1 (2019).

72. D. DellaGiustina, Maps_DellaGiustina_et_al_Science_2020_abc3660. figshare (2020); https://doi.org/10.6084/m9.figshare.12996494.

73. J. Y. Li *et al*., "Asteroid photometry" *Asteroids IV*, 129–150 (2015).

74. L. Keszthelyi *et al*., Support and future vision for the integrated software for imagers and spectrometers (ISIS). *Lunar and Planetary Science Conference* 44 (2013).

75. Principal component analysis of raw data. www.mathworks.com/help/stats/pca.html.

76. L. Scrucca, M. Fop, T. B. Murphy, A. E. Raftery, mclust 5: Clustering, classification and density estimation using Gaussian finite mixture models. *R J.* **8**, 289–317 (2016). doi:10.32614/RJ-2016-021 Medline

77. S. J. Bus, R. P. Binzel, Phase II of the small main-belt asteroid spectroscopic survey: A feature-based taxonomy. *Icarus* **158**, 146–177 (2002). doi:10.1006/icar.2002.6856

78. C. M. Ernst *et al*., The Small Body Mapping Tool (SBMT) for accessing, visualizing, and analyzing spacecraft data in three dimensions. *Lunar and Planetary Science Conference* 49 (2018).

79. W. F. Bottke Jr., M. C. Nolan, R. Greenberg, R. A. Kolvoord, Velocity distributions among colliding asteroids. *Icarus* **107**, 255–268 (1994). doi:10.1006/icar.1994.1021

80. E. Tatsumi, T. Kouyama, H. Suzuki, M. Yamada, N. Sakatani, S. Kameda, Y. Yokota, R. Honda, T. Morota, K. Moroi, N. Tanabe, H. Kamiyoshihara, M. Ishida, K. Yoshioka, H. Sato, C. Honda, M. Hayakawa, K. Kitazato, H. Sawada, S. Sugita, Updated inflight

calibration of Hayabusa2's optical navigation camera (ONC) for scientific observations during the cruise phase. *Icarus* **325**, 153–195 (2019). doi:10.1016/j.icarus.2019.01.015

81. L. B. Browning, H. Y. McSween Jr., M. E. Zolensky, Correlated alteration effects in CM carbonaceous chondrites. *Geochim. Cosmochim. Acta* **60**, 2621–2633 (1996). doi:10.1016/0016-7037(96)00121-4

82. P. R. Buseck, X. Hua, Matrices of carbonaceous chondrite meteorites. *Annu. Rev. Earth Planet. Sci.* **21**, 255–305 (1993). doi:10.1146/annurev.ea.21.050193.001351

83. M. E. Zolensky, R. A. Barrett, L. Browning, Mineralogy and composition of matrix and chondrule rims in carbonaceous chondrites. *Geochim. Cosmochim. Acta* **57**, 3123–3148 (1993). doi:10.1016/0016-7037(93)90298-B

84. K. T. Howard, G. K. Benedix, P. A. Bland, G. Cressey, Modal mineralogy of CM chondrites by X-ray diffraction (PSD-XRD): Part 2. Degree, nature and settings of aqueous alteration. *Geochim. Cosmochim. Acta* **75**, 2735–2751 (2011). doi:10.1016/j.gca.2011.02.021

85. E. A. Cloutis, M. J. Gaffey, T. F. Moslow, Spectral reflectance properties of carbon-bearing materials. *Icarus* **107**, 276–287 (1994). doi:10.1006/icar.1994.1023

86. E. A. Cloutis, T. Hiroi, M. J. Gaffey, C. M. O. D. Alexander, P. Mann, Spectral reflectance properties of carbonaceous chondrites: 1. CI chondrites. *Icarus* **212**, 180–209 (2011). doi:10.1016/j.icarus.2010.12.009

87. E. A. Cloutis, P. Hudon, T. Hiroi, M. J. Gaffey, P. Mann, Spectral reflectance properties of carbonaceous chondrites: 2. CM chondrites. *Icarus* **216**, 309–346 (2011). doi:10.1016/j.icarus.2011.09.009

88. V. K. Pearson, M. A. Sephton, I. A. Franchi, J. M. Gibson, I. Gilmour, Carbon and nitrogen in carbonaceous chondrites: Elemental abundances and stable isotopic compositions. *Meteorit. Planet. Sci.* **41**, 1899–1918 (2006). doi:10.1111/j.1945-5100.2006.tb00459.x

89. A. R. Hildebrand, L. Hanton, M. Rankin, M. I. Ibrahim, (2015) An asteroid regolith simulant for hydrated carbonaceous chondrite lithologies (HCCL-1). 78th Meteoritical Society Meeting; abstract #5368.

90. T. K. Croat, T. Bernatowicz, S. Amari, S. Messenger, F. J. Stadermann, Structural, chemical, and isotopic microanalytical investigations of graphite from supernovae. *Geochim. Cosmochim. Acta* **67**, 4705–4725 (2003). doi:10.1016/S0016-7037(03)00463-0

91. C. El Amri, M.-C. Maurel, G. Sagon, M.-H. Baron, The micro-distribution of carbonaceous matter in the Murchison meteorite as investigated by Raman imaging. *Spectrochim. Acta A* **61**, 2049–2056 (2005). doi:10.1016/j.saa.2004.08.005 Medline